EVALUATION OF A METHOD OF CRUSTAL EXPLORATION

BASED ON CONVERTED WAVES FROM MICROEARTHQUAKES

A thesis presented to the faculty of the

New Mexico Institute of Mining and Technology

in partial fulfillment of the requirements for the

Degree of Master of Science in Geophysics

by

Eric L. Berg

June 1968

ACKNOWLEDGEMENTS

TABLE OF CONTENTS

LIST OF FIGURES

LIST OF TABLES

ABSTRACT

A method of exploration of the upper crust based on the obser-
vation and identification of converted energy waves from microearthquakes
is developed. Waves generated by both P to SV and SV to P con-
versions at velocity discontinuities are taken into account. Relationships
are derived that give the depth to a velocity discontinuity in terms of
the velocity distribution within the section, the measured (PS-P) and
(S-SP) time intervals, and the angle of incidence of the parent wave at
a velocity discontinuity. The simultaneous solution of these equations
provides unique values for the depth of the interface and the depth of the
primary energy source. An error analysis indicates that the plane wave
approximation and the assumption that Poisson's ratio is constant lead to
errors in the depth calculation of only a few percent.

Field recordings of microearthquakes were made near Socorro to
test the application of the method to the determination of shallow layering
in sedimentary basins. Examples of microearthquake records showing
possible converted energy arrivals are given. Spectral analysis indicates
the frequency content of the SP waves is in the 2-10 HZ. band and is
distinguishable from the frequency content of the P and PS waves which
is centered in the 10-25 HZ. band. This frequency separation is the
basis for digital filtering which, along with stacking, is used to improve
the signal-to-noise ratio of the seismograms.

An interpretation of the records based on the measured (PS-P)
and (S-SP) intervals was carried out. The calculated values of the depth
of the velocity interface, depth of the microearthquake focus, and distance
of the epicenter are within the range of expected values at each recording
station.

The operation of three-component recording equipment in an array
of recording stations is a recommended means of improving the detection

of converted energy waves from microearthquakes. In basinal areas located near current microearthquake activity, the interpretation of the converted energy arrivals in terms of depths of velocity discontinuities could provide an economical way of finding the general shape, size, and depth of the sedimentary basins.

INTRODUCTION

BACKGROUND OF PREVIOUS INVESTIGATIONS

The incidence of a seismic wave upon the boundary separating two elastic media will generate both reflected and refracted waves. In general, both transverse and longitudinal waves are developed at the interface. When a compressional wave is incident at the boundary, the longitudinal energy is partitioned among a transmitted logitudinal wave, a reflected longitudinal wave, a transmitted transverse wave, and a reflected transverse wave. The latter two waves are derived from the conversion of longitudinal energy into transverse energy, and are called converted waves. In the case of incident compressional energy having a plane wavefront, the converted phases are vertically polarized shear waves or SV waves (Grant and West, 1965). The notation PS is henceforth used to denote the resultant of a P to SV energy transformation. Similiarily, an SV wave incident at a boundary generates a transmitted SV, a reflected SV, a transmitted P, and a reflected P. The latter two are converted waves. The notation SP is used to denote the resultant of an SV to P energy transformation. Horizontally polarized shear waves, or SH waves, need not be taken into consideration because; (1) SH waves are not generated by plane P or SV waves incident at a boundary, and (2) a plane SH wave striking a boundary does not generate P or SV waves.

The elastic media are considered to be homogeneous and isotropic. The overall velocity of a layer is taken to be its average velocity without regard to internal velocity gradients or discontinuities. The incident and transmitted waves are assumed to be nearly planar.

In general, the amplitude of the converted wave is a function of the velocity and density contrast at the interface and the angle the incident wave makes with the normal to the boundary. The theoretical

distribution of energies and resultant wave amplitudes for plane waves incident was first developed by Zoeppritz (McCamy, et al., 1962).

The appearance of significant energy in converted phases on various seismograms has been reported by Meissner (1965) who treated converted wave arrivals as unwanted multiples observed in refraction shooting. The interpretation of converted energy arrivals as a possible means of determination of crustal structure was proposed by G. A. Gamburtsev in 1939 (Gal'perin and Frolova, 1966). Andrev in 1957 (Schwind, et al., 1957) renewed the interest in converted energy as a means of study of deep crustal structure. V. N. Gaiskli studied seismograms of distant earthquakes showing converted PS energy arrivals generated by the reflection of SV waves at a boundary (Mishin and Dareshkina, 1966). Schwind et al. (1957) applied the method, using only PS conversions from explosion sources, to crustal layering with good results.

In summation, published accounts of previous research in this field have, in general, the following characteristics:
(1) The emphasis was placed on the observation and analysis of PS converted waves without consideration of the SP phases.
(2) The energy source was either a distant earthquake or explosion located on the order of a few hundreds of kilometers from the detector.
(3) The method was applied to the problem of detection of gross crustal structures at depth and not to individual layering of possible economic significance within the sedimentary veneer.

OBJECTIVES OF RESEARCH

The purpose of this thesis is to outline and evaluate a proposed method of exploration of the upper crust based on the joint interpretation of PS and SP transmission-type converted energy arrivals identified on the seismograms of local microearthquakes. The basic methods outlined

in this research could have direct applications in geophysical exploration programs as an inexpensive means of obtaining reconnaissance surveys of the thickness and shape of sedimentary basins.

The SP converted phase which has been largely ignored in previous studies is identifiable on the seismograms of local microearthquakes near Socorro having (S-P) intervals less than four seconds. The measurement of two independent variables, the (PS-P) and (S-SP) intervals, then leads to a more reliable structural interpretation. The proximity of the energy source of Socorro microearthquakes provides strong S energy and thus the possibility of identifiable SP phases.

The microearthquake activity near Socorro provides an energy source at an average depth of about five kilometers (Sanford and Long, 1965). The microearthquakes have epicentral distances of from two to 40 kilometers from Socorro. Inasmuch as the energy source in the present study lies below the velocity discontinuities of interest, emphasis will be placed on the identification of transmitted converted phases. Reflected converted energy will be of no consequence except in the case of internal reflection of converted waves within the sedimentary layering. The multiple-type arrivals generated in this manner may be a source of background noise between the arrival of P and S phases which could explain the continuing ground unrest after passage of the initial P-wave.

Within the Socorro microearthquake area lie the Rio Grande graben and Snake Ranch trough. Both constitute areas of sedimentary deposition in physiographic basins. The methods of interpretation outlined in this thesis are applied to the problem of determination of the thickness of individual sedimentary layers within these basins.

THEORY

AMPLITUDE CONSIDERATIONS

The observed amplitudes of refracted and converted wave arrivals on the seismogram are directly related to the partition of the incident wave amplitude at the velocity interface. The Zoeppritz amplitude equations describe this partition for plane waves. Solutions of the Zoeppritz relationships for various physical parameters have been graphically presented by McCamy et al. (1962). The curves of McCamy furnish ratios of resultant wave amplitudes to incident wave amplitudes in the form $\overline{PS}_1/\overline{P}_2$, $\overline{P}_1/\overline{P}_2$, $\overline{SP}_1/\overline{S}_2$, and $\overline{S}_1/\overline{S}_2$ where $\overline{PS}_1$, $\overline{SP}_1$, $\overline{P}_1$, $\overline{S}_1$, $\overline{P}_2$, and $\overline{S}_2$ are the amplitudes of the PS converted waves, SP converted waves, refracted P, refracted SV, incident P, and incident SV waves, respectively.

The numerical results of McCamy can be used to form the $\overline{PS}_1/\overline{P}_1$ and $\overline{SP}_1/\overline{S}_1$ relationships which are the expected amplitude ratios of the PS converted wave to P wave and SP converted wave to SV wave which should be observed on the seismogram. Figure 1 shows a set of curves of the expected amplitude ratios for velocity contrasts across the interface ranging from $R = 0.52$ to $R = 1.09$ where $R = VP_1/VP_2$ is the ratio of the compressional velocity in the refracting medium to the compressional velocity in the incident medium. The specific velocity and density ratios used and their corresponding curve numbers are summarized in Table 1. Poisson's ratio was taken to be 0.25.

The criteria for limiting angles of incidence listed in Table 2 denote the maximum angle of incidence at a given interface for which the specified secondary wave types are generated. The curves of Figure 1 are compiled only for those angles of incidence for which both wave types necessary to form the amplitude ratio are developed.

Table 1. Curve numbers and corresponding physical
parameters for the relationships of converted and
direct wave amplitudes shown in Figure 1.

CURVE	VELOCITY RATIO	DENSITY RATIO
1	0.52	0.76
2	0.52	0.76
3	0.71	0.83
4	0.71	0.83
5	0.83	0.89
6	0.83	0.89
7	1.09	1.05
8	1.09	1.05

Odd numbered curves are for PS/P ratios.

Even numbered curves are for SP/S ratios.
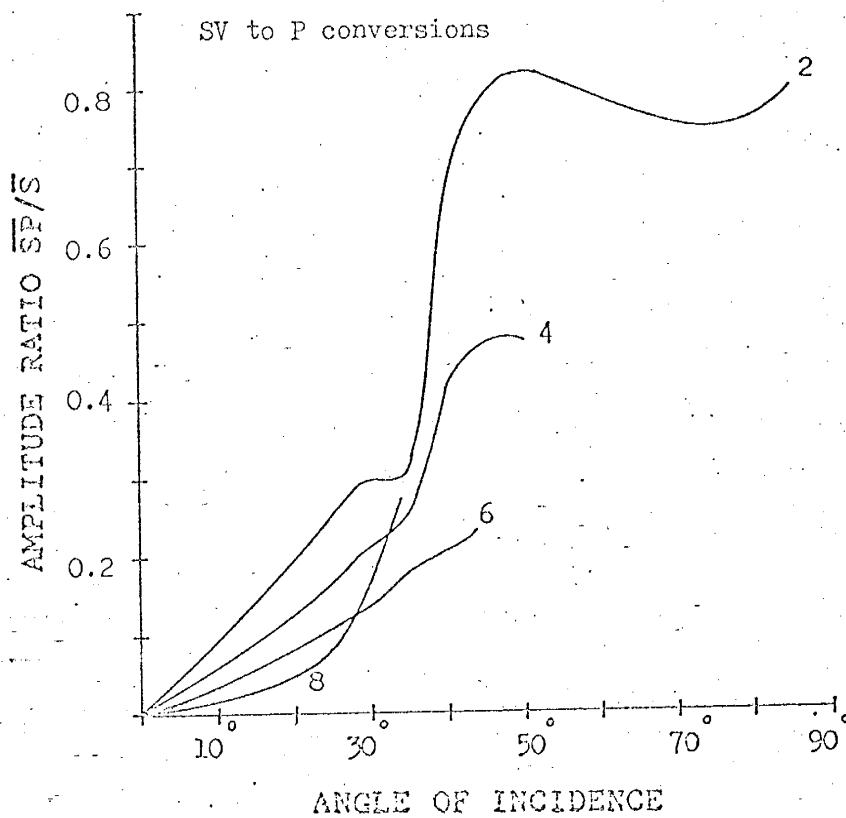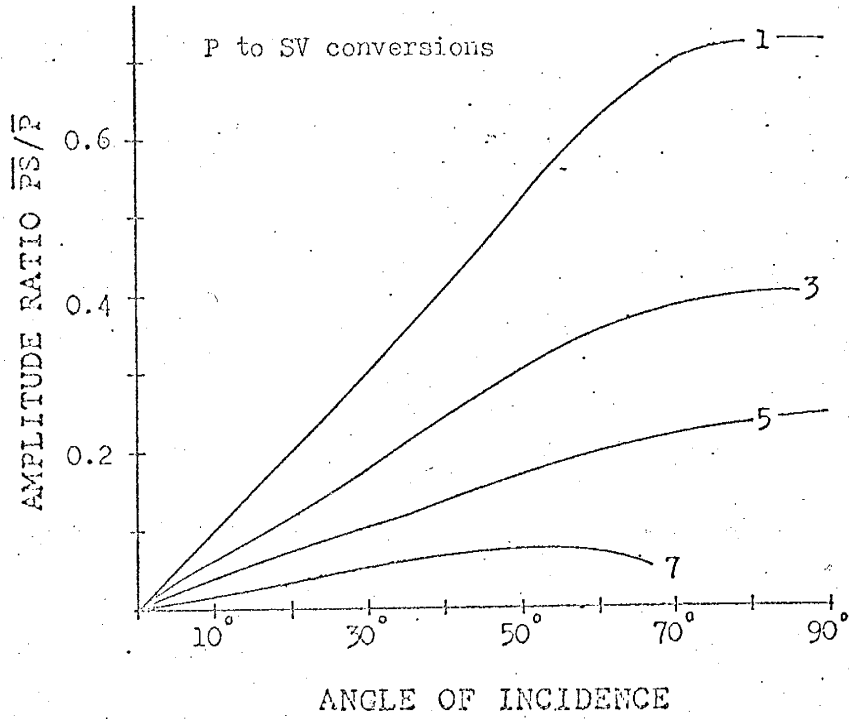
Figure 1. Converted/refracted wave amplitude ratios versus angle of incidence and velocity ratio.

Table 2. Criteria for determining limiting angles.

INTERFACE	WAVE TYPE	LIMITING ANGLE OF INCIDENCE
$VP_1 > VP_2$	P_1, S_1	$\sin^{-1}(VP_2/VP_1) = \sin^{-1}(VS_2/VS_1) = 1/R$
$VP_1 > VP_2$	SP_1	$\sin^{-1}(VS_2/VP_1) = 1/(\sqrt{3}R)$
$VS_1 > VP_2$	PS_1	$\sin^{-1}(VP_2/VS_1) = \sqrt{3}/R$
$VP_2 > VP_1$	P_1, S_1, PS_1	Always Formed

The curves of Figure 1 show that significant converted wave amplitudes can be generated at reasonable velocity discontinuities. The amplitude ratio is generally higher with increasing angle of incidence and decreasing R. The SP converted wave amplitudes will be larger than the corresponding PS amplitudes because $\overline{SP}/\overline{S} > \overline{PS}/\overline{P}$ and $\overline{S} > \overline{P}$. The velocity criteria and limiting angle of incidence for the formation of SP waves are, however, much more restrictive than for the generation of PS waves. In the case where $VP_1 > VP_2$, even if the velocity reversal is slight as in curves 7 and 8 of Figure 1, the formation of converted energy is limited to small angles of incidence for which the resultant amplitudes are small. In general, $R < 1.2$ is a necessary condition for observation and identification of converted waves, and $R < 0.6$ is an optimum condition.

CALCULATION OF DEPTH OF INTERFACE BASED ON (PS-P)

The ray path for a compressional wave, P_1, refracted at a velocity interface is shown in Figure 2 as FAB. As the incident compressional wave, P_2, strikes the interface, a conversion of energy takes place and a secondary wave, a vertically polarized shear wave or SV wave, is propagated in the second medium. The ray path for the arrival of converted P to SV energy, PS_1, is FCDB. The time interval (PS-P) is measured directly on the seismic record as the time lag between the P_1 and later PS_1 signals. This delay time is given by

$$(PS-P) = (FC/VP_2 + CD/VP_2 + DB/VS_1) - (FA/VP_2 + AB/VP_1) \ . \qquad (1)$$

The PS_1 wavefront is the Huygen's envelope of those secondary shear wavelets, generated all along the velocity discontinuity, which are in phase at the time of arrival of converted PS_1 energy at the seismometer. The arrival at point E of the wavelet which was generated at point A exactly

Figure 2. Geometry and nomenclature for P to SV energy conversions at a velocity discontinuity.

coincides in time with the arrival at the detector of the wavelet generated at point D. Ray paths AE and DB are normal to the PS_1 wavefront. The following travel time relation holds from the geometry

$$FC/VP_2 + CD/VP_2 + DB/VS_1 = FA/VP_2 + AE/VS_1 \qquad (2)$$

A and C are points on the same P_2 wavefront, and FC = FA. Now equation (2) reduces to

$$CD/VP_2 + DB/VS_1 = AE/VS_1 . \qquad (3)$$

Substituting (3) into (1) gives

$$(PS-P) = AE/VS_1 - AB/VP_1 . \qquad (4)$$

The approximation is made here that the incident P_2 wave is nearly planar at its contact with the velocity interface, and therefore the BE segment of the PS_1 wavefront is nearly planar such that angle AEB approaches 90°.
Then from Figure 1,

$$\cos (iPP_1 - iPS_1) = AE/AB, \qquad (5)$$

and

$$\cos (iPP_1) = Z_1/AB . \qquad (6)$$

Substituting (5) and (6) into (4) gives

$$(PS-P) = \frac{Z_1}{\cos(iPP_1)} \left[\frac{\cos(iPP_1 - iPS_1)}{VS_1} - \frac{1}{VP_1} \right] . \qquad (7)$$

10

The relationship in equation (7) is given without detailed derivation by Meisser (1965). For the generally applicable case where Poisson's ratio can be assumed to be 0.25, the ratio of V_p/V_s remains constant at $\sqrt{3}$ and

$$(PS-P) = \frac{Z_1}{VP_1 \cos(iPP_1)} \left[\sqrt{3} \cos(iPP_1 - iPS_1) - 1 \right] . \tag{8}$$

Solving for Z_1,

$$Z_1 = (PS-P) \cdot VP_1 \cdot \cos(iPP_1) / \left[\sqrt{3} \cos(iPP_1 - iPS_1) - 1 \right] . \tag{9}$$

After the substitution of two trigonometry identities, equation (9) may be rearranged in the form

$$Z_1 = (PS-P) \cdot VP_1 / \left[\sqrt{3} \cos(iPS_1) - \cos(iPP_1) \right] . \tag{10}$$

Equation (10) is given by Schwind et al. (1960).

The angular relationships given by Snell's law are as follows:

$$\sin(iPP_2) / VP_2 = \sin(iPP_1) / VP_1 = \sin(iPS_1) / VS_1 . \tag{11}$$

Equation (11) can now be expressed in terms of the angle of incidence of P_2 at the interface and the ratio of compressional velocities, $R = VP_1/VP_2$, across the interface

$$Z_1 = (PS-P) \cdot VP_1 / \left[\sqrt{3} \sqrt{1 - \frac{R^2}{3} \sin^2(iPP_2)} - \sqrt{1 - R^2 \sin^2(iPP_2)} \right] . \tag{12}$$

CALCULATION OF DEPTH OF INTERFACE BASED ON (S-SP)

The procedure for analyzing the SV to P conversion phase is similar to that used in the discussion of P to SV conversions. Figure 2

Figure 3. Geometry and nomenclature for SV to P energy conversion at a velocity discontinuity.

shows the ray path for a refracted SV arrival, S_1, labeled FCAB. The ray path for SP_1 energy arriving at the seismometer from the conversion of SV to P at the interface is labeled FD'B. In this case, the measured time interval (S-SP) is the time lag between the SP_1 and the direct S_1 arrivals. This time interval is given by the equation

$$(S\text{-}SP) = (FC/VS_2 + CA/VS_2 + AB/VS_1) - (FD'/VS_2 + D'B/VP_1) \,. \quad (13)$$

Points B and E' both lie on the SP_1 wavefront such that

$$(S\text{-}SP) = (FC/VS_2 + CA/VS_2 + AB/VS_1) - (FC/VS_2 + CA/VS_2 + AE'/VP_1) . \quad (14)$$

Equation (13) reduces to

$$(S\text{-}SP) = (AB/VS_1 - AE'/VP_1) \,. \quad (15)$$

As before, the approximation that angle AE'B approaches 90° is envoked and

$$\cos(SP_1 - iSS_1) = AE'/AB \,, \quad (16)$$

and

$$\cos(iSS_1) = Z_1/AB \,. \quad (17)$$

Substituting (16) and (17) into (15) gives

$$(S\text{-}SP) = \left[Z_1/\cos(iSS_1) \right] \left[\frac{1}{VS_1} - \frac{\cos(iSP_1 - iSS_1)}{VP_1} \right] \,. \quad (18)$$

13

The relationship in equation (18) is also given by Meissner (1965) without detailed derivation. Assuming the constant-velocity ratio $VP/VS = \sqrt{3}$, equation (18) becomes

$$(S\text{-}SP) = \frac{Z_1}{VP_1 \cdot \cos(iSS_1)} \left[\sqrt{3} - \cos(iSP_1 - SS_1) \right] . \qquad (19)$$

Solving (19) for Z_1 gives

$$Z_1 = (S\text{-}SP) \cdot VP_1 \cdot \cos(iSS_1) / \left[\sqrt{3} - \cos(ISP_1 - iSS_1) \right] . \qquad (20)$$

Since Poisson's ratio is taken as a constant, the shear velocity at the interface will be the same as the compressional velocity ratio, and angle iSS_1 in Figure 2 will equal iPP_1 in Figure 1 for any given angle of incidence. $\sin iSP_1 = \sqrt{3} \sin iPS_1$. Snell's Law for SV to P conversion is written

$$\sin(iSS_2) / VS_2 = \sin(iSS_1) / VS_1 = \sin(iSP_1) / VP_1 . \qquad (21)$$

From the relationships in equation (21) and an appropriate trigonometric identity, equation (20) may be rearranged in the form

$$Z_1 = (S\text{-}SP) \cdot VP_1 / \left[\sqrt{3} \cos(iSS_1) - \cos(iSP_1) \right] . \qquad (22)$$

By substituting equation (21) and trigonometric identities into (22) an expression for the depth of the velocity discontinuity can be obtained in terms of the angle of incidence, iSS_1 of S_2 at the interface, the (S-SP) interval, the velocity ratio R across the interface, and the compressional velocity of the upper layer.

$$Z_1 = (S\text{-}SP) \cdot VP_1 / \left[\sqrt{3} \sqrt{1 - R^2 \sin^2(iSS_2)} - \sqrt{1 - 3R^2 \sin^2(iSS_2)} \right] . \qquad (23)$$

14

From Figures 1 and 2, it is apparent that angle iPP_2 and iSS_2 are the same. These angles may therefore be replaced by i, the angle of incidence of the parent wave at the interface. Then equations (12) and (23) can be written

$$Z_1 = (PS-P) \ VP_1 / \left[\sqrt{3} \ \sqrt{1 - \frac{R^2}{3} \ \sin^2(i)} - \sqrt{1 - R^2 \sin^2(i)} \ \right] \quad (24)$$

and

$$Z_1 = (S-SP) \ (VP_1) / \left[\sqrt{3} \ \sqrt{1 - R^2 \sin^2(i)} - \sqrt{1 - 3R^2 \sin^2(i)} \ \right] . \quad (25)$$

When both the PS and SP converted energy arrivals can be identified and the (PS-P) and (S-SP) intervals measured on the seismogram, the simultaneous solution of equations (24) and (25) for Z, provide a unique determination of the depth of the interface independent of the location of the source. The numerical solutions can best be carried out graphically.

Dependence of Calculated Depth Upon i and R

Figures 4 through 7 show the dependence of the calculated depth to the interface Z_1, upon the angle of incidence, i, and the velocity ratio across the interface, R. The location of the energy source is related to the angle of incidence. The overburden velocity was held constant at 10,000 ft./sec. and the sub-interface velocity was varied such that velocity contrasts (VP_1/VP_2) of from 0.1 to 3.0 across the interface were considered. For each calculation, Poisson's ratio was taken to be 0.25 in both the first and second layer. The ordinate values are the computed depths per 0.1 second of the time intervals, (PS-P) and (S-SP).

The absolute values of Z_1 are directly proportional to the overburden velocity and time intervals. In order to correct the curves for any

15

other overburden velocity, one need only multiply the ordinate values of the curve for the velocity contrast of interest by the ratio of the desired overburden velocity to 10,000 ft./sec. To correct for any other time lag, multiply the ordinate values of the curve of interest by the ratio of the measured time lag to 0.1 second. Figures 4 through 7 are drawn only for those angles of incidence at which converted waves are developed. The limiting values of the angle of incidence listed in Table 2 can be given as functions of R alone, indicating that the modification of any curve to another overburden velocity or measured time delay will not change the value of its limiting angle.

In Figure 4, odd-numbered curves 1 through 19 are drawn for P to SV conversions where $VP_1 < VP_2$. This set of curves indicates that for values of $R < 0.6$, good estimates of Z_1 can be obtained on the basis of the (PS-P) interval alone. At large angles of incidence for which the $\overline{PS}/\overline{P}$ amplitude ratio is large (see Figure 1) the variation of the calculated value of Z_1 with angle of incidence is steep. As R is increased, the rate of change of Z_1 is also increased.

Even-numbered curves 2 through 20 in Figure 5 are drawn for SV to P conversions where $VP_1 < VP_2$. Good estimates of the depth obtained solely on the basis of the measured (S-SP) interval can be made only when $R < 0.4$ which would constitute a somewhat unrealistic velocity distribution. Therefore Z_1 cannot be reliably estimated from the (S-SP) interval alone. The calculation of Z_1 must be on the basis of the simultaneous solution of equations (24) and (25) and will be limited to angles of incidence smaller than the limiting angle for SP conversions.

The family of odd-numbered curves 21 through 43 in Figure 6 drawn for the case of a velocity reversal within the stratigraphic section for which $VP_1 > VP_2$. The depth calculation is increasingly sensitive to the angle of incidence as i approaches the limiting angle for PS conversions.

Table 9. Curve numbers and corresponding physical parameters for the
curves in Figures 4 through 7.

CURVE NUMBER	VP_2	VP_1	R
1	100,000	10,000	.1
2	100,000	10,000	.1
3	50,000	10,000	.2
4	50,000	10,000	.2
5	33,333	10,000	.3
6	33,333	10,000	.3
7	25,000	10,000	.4
8	25,000	10,000	.4
9	20,000	10,000	.5
10	20,000	10,000	.5
11	16,667	10,000	.6
12	16,667	10,000	.6
13	14,286	10,000	.7
14	14,286	10,000	.7
15	12,500	10,000	.8
16	12,500	10,000	.8
17	11,111	10,000	.9
18	11,111	10,000	.9
19	10,000	10,000	1.0
20	10,000	10,000	1.0
21	9,091	10,000	1.1
22	9,091	10,000	1.1
23	8,333	10,000	1.2
24	8,333	10,000	1.2
25	7,692	10,000	1.3
26	7,692	10,000	1.3
27	7,143	10,000	1.4
28	7,143	10,000	1.4
29	6,667	10,000	1.5
30	6,667	10,000	1.5
31	6,250	10,000	1.6
32	6,250	10,000	1.6
33	5,882	10,000	1.7
34	5,882	10,000	1.7
35	5,556	10,000	1.8
36	5,556	10,000	1.8
37	5,263	10,000	1.9
38	5,263	10,000	1.9
39	5,000	10,000	2.0
40	5,000	10,000	2.0
41	4,000	10,000	2.5
42	4,000	10,000	2.5
43	3,333	10,000	3.0
44	3,333	10,000	3.0

Odd numbered curves correspond to P to SV conversions.

Even numbered curves correspond to SV to P conversions.

Figure 4. Computed depth of velocity discontinuity based on (PS-P) interval versus angle of incidence for the case where $VP_1 < VP_2$.

Figure 5. Computed depth of velocity discontinuity based on (S-SP) interval versus angle of incidence for the case where $VP_1 < VP_2$.
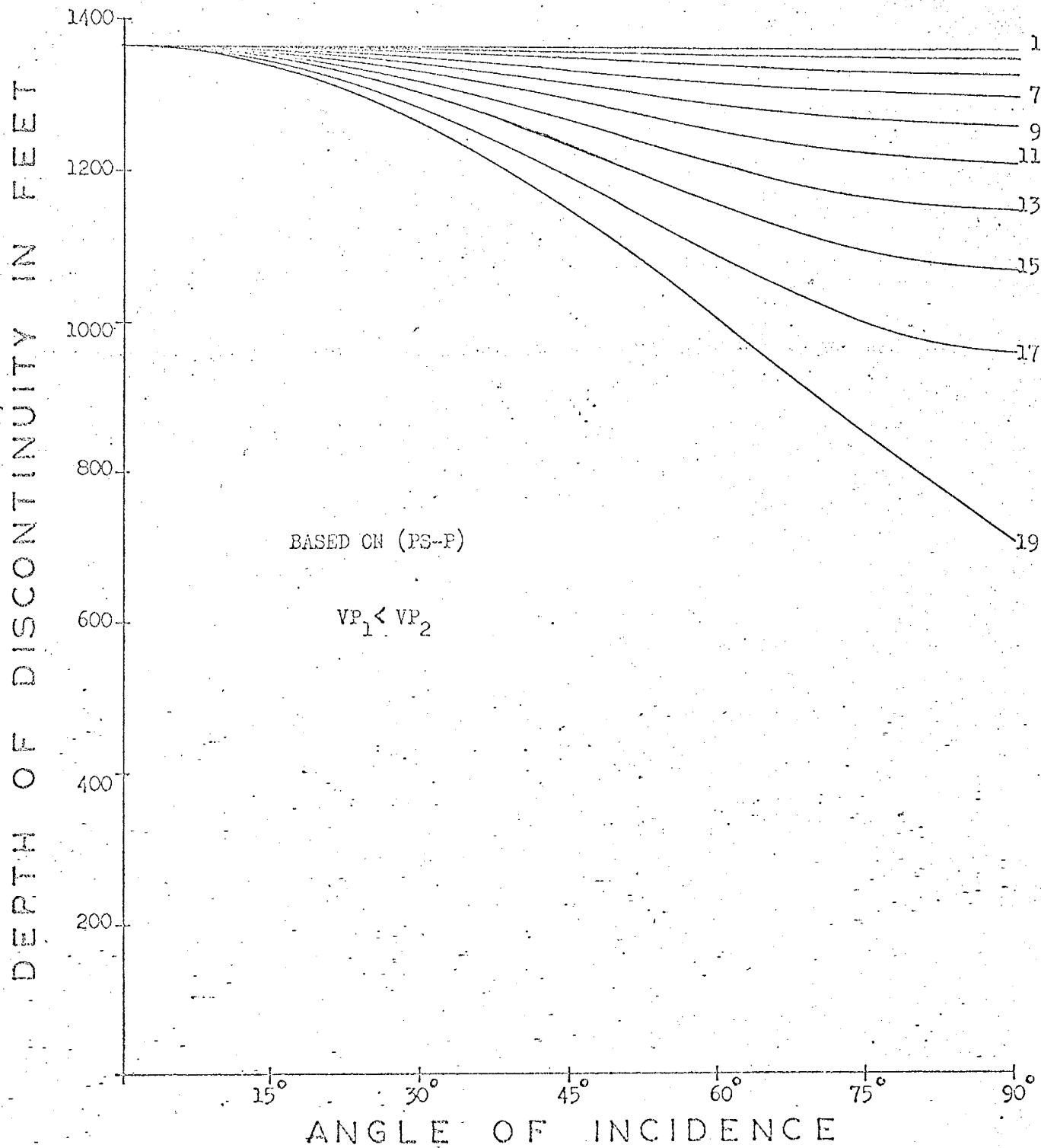
Figure 6. Computed depth of velocity discontinuity based on (PS-P) interval versus angle of incidence for the case where $VP_1 > VP_2$.

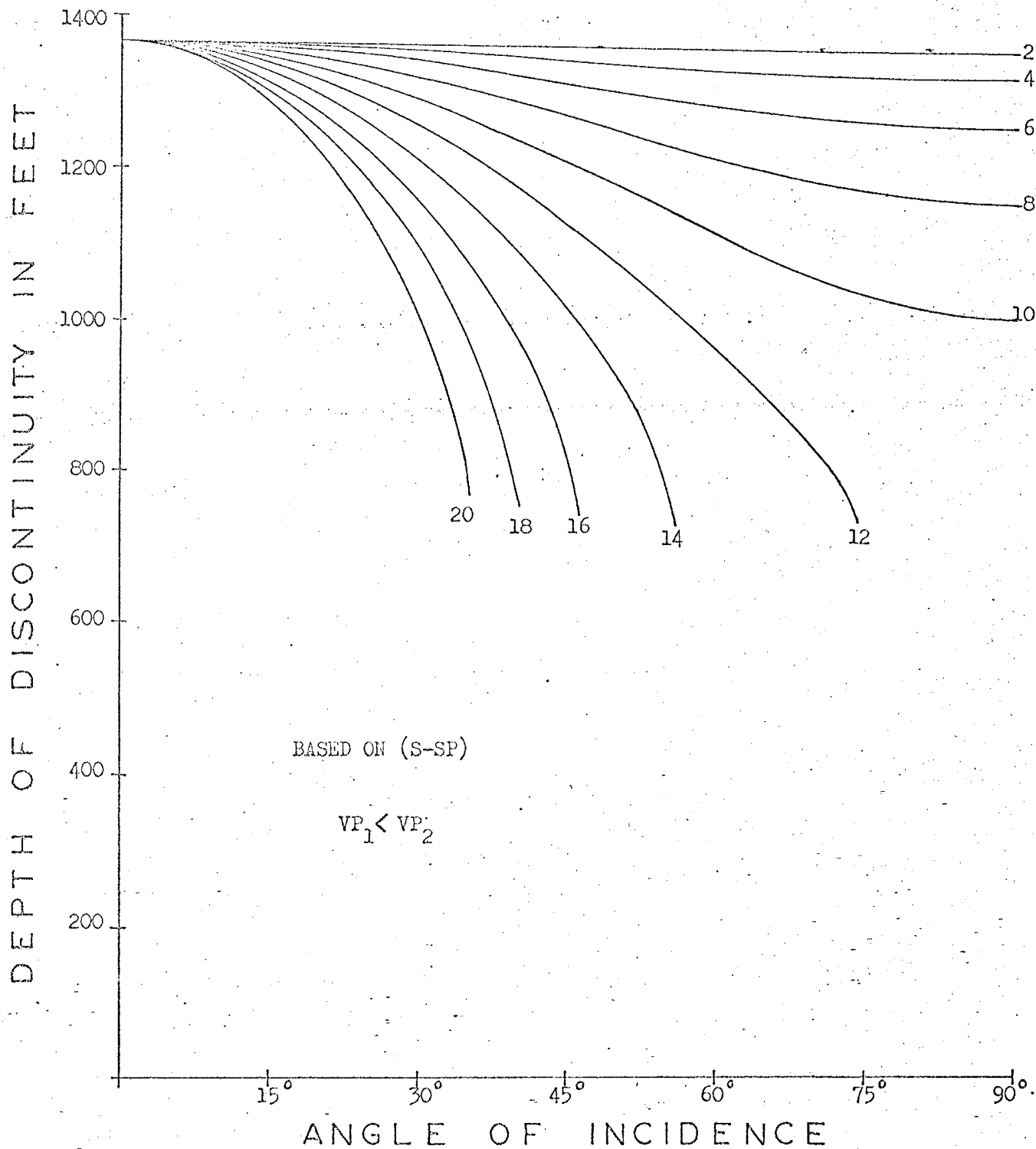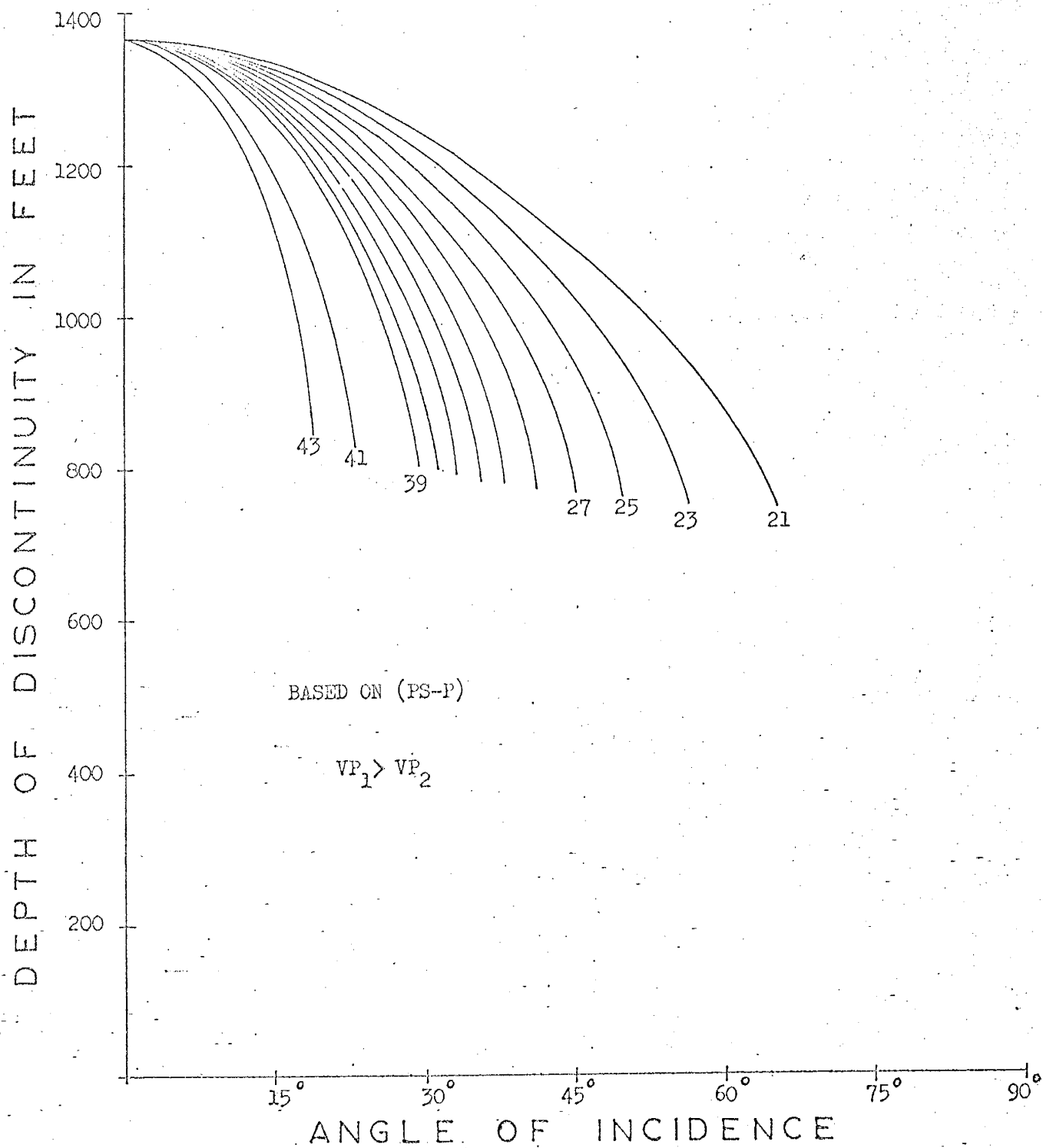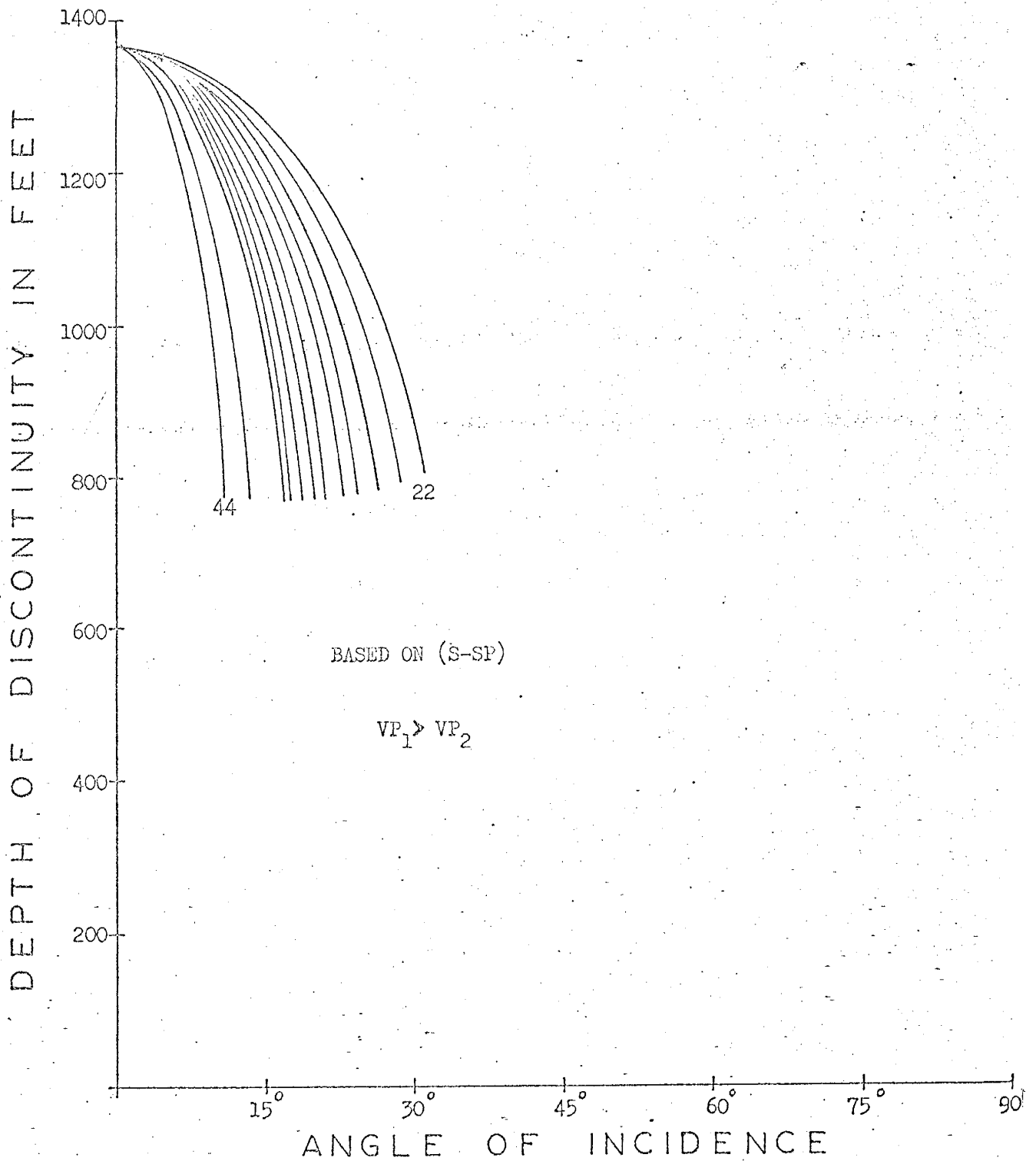Figure 7. Computed depth of velocity discontinuity based on (S-SP) interval versus the angle of incidence for the case where $VP_1 > VP_2$.

As shown by the steepness of these curves, any determination of the depth of a velocity reversal must be verified by calculations based on both the (PS-P) and (S-SP) interval.

Figure 7 shows even-numbered curves 22 through 44 which are drawn for SV to P conversions at a velocity reversal. The calculation of Z_1 is very sensitive to the angle of incidence and is curtailed by the limiting angle for SP conversions.

In all cases the rate of change of the calculated depth of the discontinuity increases with the angle of incidence and velocity ratio across the interface. The value of Z_1, when based on the (PS-P) interval is less sensitive to i and R and therefore more reliable than when based on the (S-SP) interval. The depth calculation is also less sensitive to i and R and therefore more reliable when $R < 1.0$.

Error Due To Plane Wave Assumption

The approximations leading to equations (7) and (14) above that angle AEB approaches 90° infers that the tangent constructed to the PS_1 wavefront at point E also intersects the detector, or that points G and B in Figure 2 coincide. This approximation is good for angles of incidence near the normal for which angle iPS_1 does not differ by much from angle iPP_1 and angle iSP_1 does not differ by much from iSS_1. For larger i, the calculated values of Z_1 are in error.

To examine the magnitude of the error, consider the limiting case of a spherical PS_1 wavefront. In all cases, the curvature of the PS_1 wavefront will be less than that of a sphere of radius AB centered at point A. Therefore the maximum error will always be less than the error for a spherical wavefront.

$$e < GB \cdot \cos(iPP_1) \qquad (26)$$

22

In the case of a spherical wavefront $AE = AB$, and

$$e < AB \cdot \cos(iPP_1) \left[(1/\cos(iPP_1 - iPS_1)) - 1 \right] \qquad (27)$$

which reduces to the form

$$e < Z_1 \left[\sec(iPP_1 - iPS_1) - 1 \right] \qquad (28)$$

The maximum error is at $i = 90°$ for which, by Snell's Law expressed in equation (11), $iPP_2 = \sin^{-1} (R)$, and $iPS_1 = \sin^{-1} (R/ \sqrt{3})$.

Taking $R = 0.6$, the maximum error would correspond to

$$e = \left[\sec(37° - 20°) - 1 \right] Z_1 = .046Z_1 \qquad . \qquad (29)$$

For Socorro microearthquakes at average distances greater than 20,000 feet corresponding to an (S-P) interval of one second, the error is smaller. The error is also decreased at smaller values of i, the incidence angle. For large R, however, e is increased. This error need not be of concern because of the nature of its small magnitude.

Effect of Offset of Points of Conversion Along Interface

The point of P refraction at the interface in Figure 2 and the point of SV refraction in Figure 3 are the same point, A, on the interface. The point of P to SV energy conversion, labeled D in Figure 2, and the point of SV to P energy conversion, labeled D in Figure 3, do not necessarily coincide with each other, nor do they coincide with A. In effect, the velocity discontinuity is sampled at three discrete points, A, D, and D' along the interface. The offsets of these points from a perpendicular to the interface passing through the detector are labeled X_1, X_2, and X_2'. The span of the interface which is involved in any one

23

depth determination using both types of converted energy arrivals is

$$S = Z_1 \left[\tan(iSP_1) - \tan(iPS_1) \right] . \tag{30}$$

For a maximum angle of incidence $i = 90°$ and velocity ratio $R = 0.5$, Snell's Law gives

$$iPS_1 = \arcsin \left[R \cdot \sin(i) / \sqrt{3} \right] = \arcsin 0.29 , \tag{31}$$

and

$$iSP_1 = \arcsin \left[R \cdot \sqrt{3} \sin(i) \right] = \arcsin 0.87 . \tag{32}$$

For this case, S approaches the limiting value

$$S = Z_1 \left[\tan(60°) - \tan(17°) \right] \quad 1.43 Z_1 . \tag{33}$$

For greater values of R, the maximum angle of incidence is the limiting angle (see Table 2). At smaller angles of incidence, the error is significantly reduced. For $i = 60°$, $S = 1.07 Z_1$, and for $i = 30°$, $S = .33 Z_1$.

In general, S will increase with larger R and larger i. The interface should be essentially smooth or regular between the two points of energy conversion for a valid depth determination. Structures having length shorter than S will be detected by the method, but cannot be reliably interpreted. The degree of resolving power to detect small structures increases with the magnitude of the velocity discontinuity and decreases with increasing depth of burial. It is also dependent on the angle of incidence at the interface which is controlled by the location of the primary energy source. In all but the most favorable conditions of velocity and source location, this restriction places serious limitations on the effectiveness of structual interpretations based on converted energy arrivals.

Error Due to Variations In Poisson's Ratio

Poisson's ratio, q, is the ratio of the horizontal strain to the vertical strain which a unit of rock undergoes during the application of stress. Throughout the theoretical development, Poisson's ratio was taken to be a constant equal to 0.25. This is probably a fairly good estimate of the overall average value of q for the entire section, but not necessarily for individual lithologic units. The influence of the values of Poisson's Ratio on the theoretical amplitude ratios of Figure 1 is very small, introducing only slight variations at angles of incidence approaching the limiting angle (Koefoed, 1962). The amplitude ratios are slightly lower as q is increased, but the effects appear to be small enough to be neglected.

To examine the influence of Poisson's Ratio upon the depth calculations, consider equations (10) and (22) in which the ratio of the compressional wave velocity to the shear wave velocity is $\sqrt{3}$ under the assumption that $q = 0.25$.

$$\frac{VP}{VS} = \left[(1 - q) / (\frac{1}{2} - q) \right]^{\frac{1}{2}} . \tag{34}$$

If q were increased by 20% (to $q = 0.30$), the corresponding ratio of VP/VS would be increased by just 8% to 1.87. A given change in q will produce the maximum change in Z_1 (as calculated by equations (24) and (25)) when the angle of incidence, i, approaches 90°. In this case, equation (24) reduces to the form given by equation (35),

$$Z_1 = \frac{(PS-P) \cdot VP_1}{\frac{VP}{VS} \sqrt{1 - \frac{R^2}{3}} - \sqrt{1 - R^2}} . \tag{35}$$

and a 20% increase of q will produce only a 14.5% decrease in the value of z, computed from the (PS-P) interval. At $i = 90°$, equation (25) reduces to the form given by equation (36),

$$Z_1 = \frac{(S-SP) \cdot VP_1}{\frac{VP}{VS}\sqrt{1 - R^2} - \sqrt{1 - 3R^2}} \tag{36}$$

for which a 20% increase of q will produce a 10.6% decrease in the value of z, computed from the (S-SP) interval. The percent change in z, will decrease for smaller angles of incidence.

Effect of Dip

In the case of a non-horizontal velocity interface, the effect of unknown dip on the depth determination cannot be found from the records of a single station. In the two-layer case, the solution for Z_1 from the time-delay analysis is actually the perpendicular distance from the plane of the interface to the detector regardless of the attitude of that plane. The solution for i gives the angle of incidence with the normal to the interface. Therefore the dip angle is indeterminant and the plane of the velocity discontinuity is merely defined to be tangent to a hemisphere of radius Z_1 centered at the detector. The records from two or more adjacent stations, however, determine an apparent attitude of the dipping interface between the stations. The true attitude of the interface can be uniquely determined by constructing a surface which is tangent to each hemisphere of radius Z_1 constructed for each recording station. This method of interpretation also corrects for differences in surface elevation between the individual recording sites.

DETERMINATION OF DEPTH OF ENERGY SOURCE

When both the PS and SP, converted energy arrivals can be identified on the seismogram, and the (S-P), (PS-P) and (S-SP) time
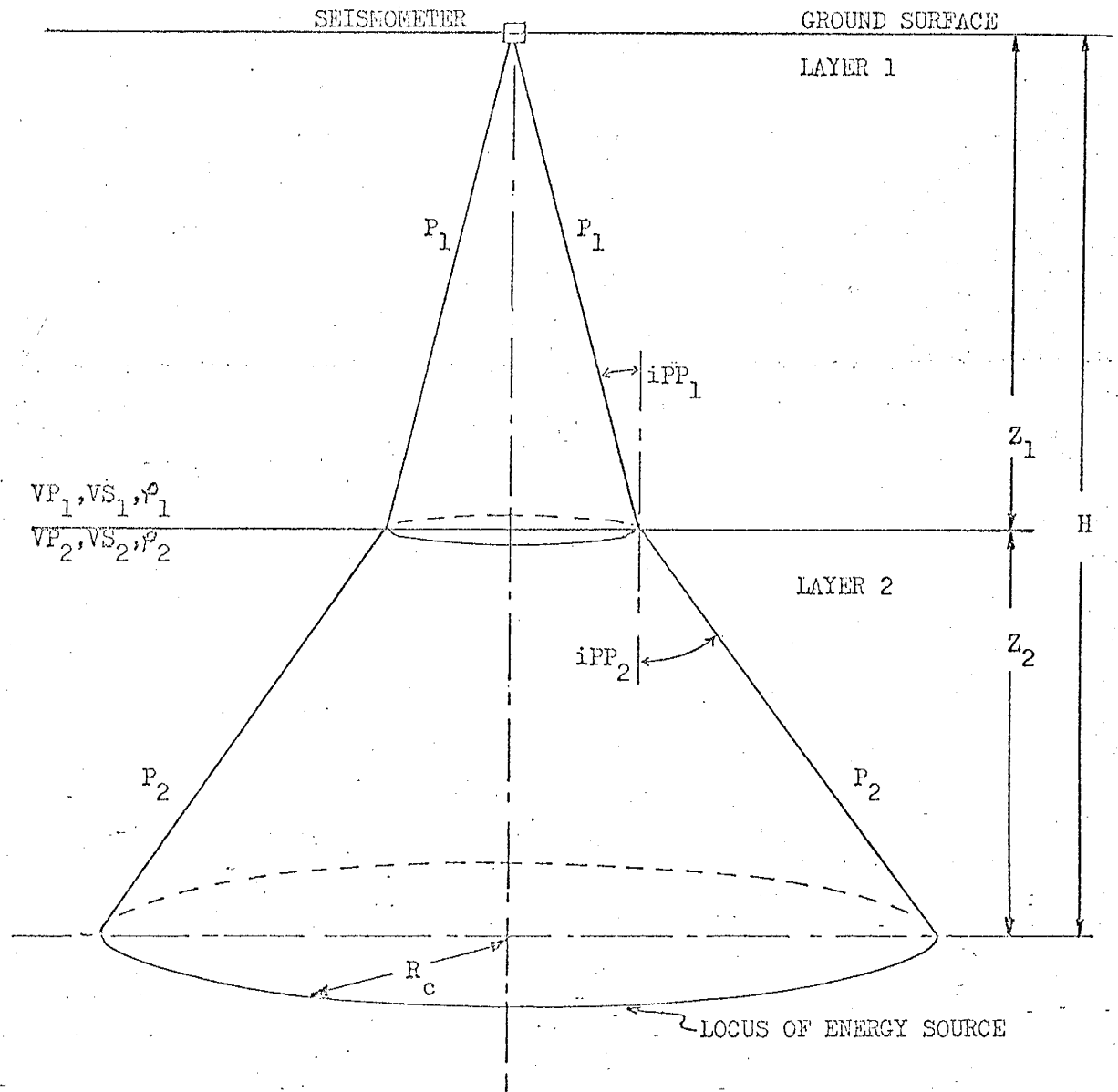
Figure 8. Geometry of source depth determination.

intervals measured, the simultaneous solution of equations (24) and (25) for Z_1, also provides a unique determination of the angle of incidence by means of which the depth of the primary energy source can be found. The (S-P) time interval can be used to determine the total distance D, from source to detector by the well-known expression:

$$D = 1.37 (S-P) \cdot \overline{VP} \quad . \tag{37}$$

where $\overline{VP}$ is the average compressional wave velocity from the source to the seismometer and Poisson's Ratio is taken to be 0.25. From the geometry of Figure 3, D is also given by

$$D = Z_1/\cos(iPP_1) + Z_2/\cos(iPP_2) . \tag{38}$$

The numerical values of Z_1, iPP_1, iPP_2 are obtained from the solution of equations (24) and (25) and Snell's Law.

By the analysis of converted energy arrivals on the seismogram of a single detector, the focus can be determined to lie somewhere on a horizontal circle of radius R_c, centered directly beneath the seismometer. The focal depth of the energy source, H, is given by

$$H = Z_1 + Z_2 . \tag{39}$$

Substituting (37) into (38) and solving for Z_2, equation (39) may be written

$$H = Z_1 + \cos(iPP_2) \left[1.37(S-P) \, VP - Z_1/\cos(iPP_1) \right] . \tag{40}$$

The radius R_c is given by equation (41).

$$R_c = Z_1 \tan(iPP_1) + Z_2 \tan(iPP_2) .$$ (41)

After substitution for Z_2, obtain (42)

$$R_c = Z_1 \tan(iPP_1) + \tan(iPP_2)\cos(iPP_2) \left[1.37(S-P) VP - Z_1/\cos(iPP_1) \right] .$$ (42)

A single, vertical seismometer, however, can provide no indication as to the azimuth of energy arrivals in an isotropic medium.

EXTENSION OF THE THEORY TO MULTIPLE LAYERING

Depth of Nth Interface Based on (PS-P)

The foregoing discussion has been directed to the case of a two-layer section. Consider now the section consisting of $N + 1$ conformable layers numbered from 1 at the surface to $N + 1$ at the source. A PS converted wave formed at the base of the surface layer would be denoted as PS_1, and the PS converted wave formed at the base of the N-th layer would be designated as PS_N. Figure 9 shows the geometry and nomenclature of a PS_N converted wave in a section modeled by $N + 1$ layers.

The actual ray path for a PS_N converted wave is FDB. By the same argument that led to equation (3), ray path FAE is an equal time path for the PS_N wave. Ray path FAB is for the propagation of the transmitted P-wave. The measured time interval (PS_N-P) is the observed time lag between the arrival of the direct P-wave and the later arrival of the converted PS_N wave. The time delay due to the passage of both waves through the jth layer is given by

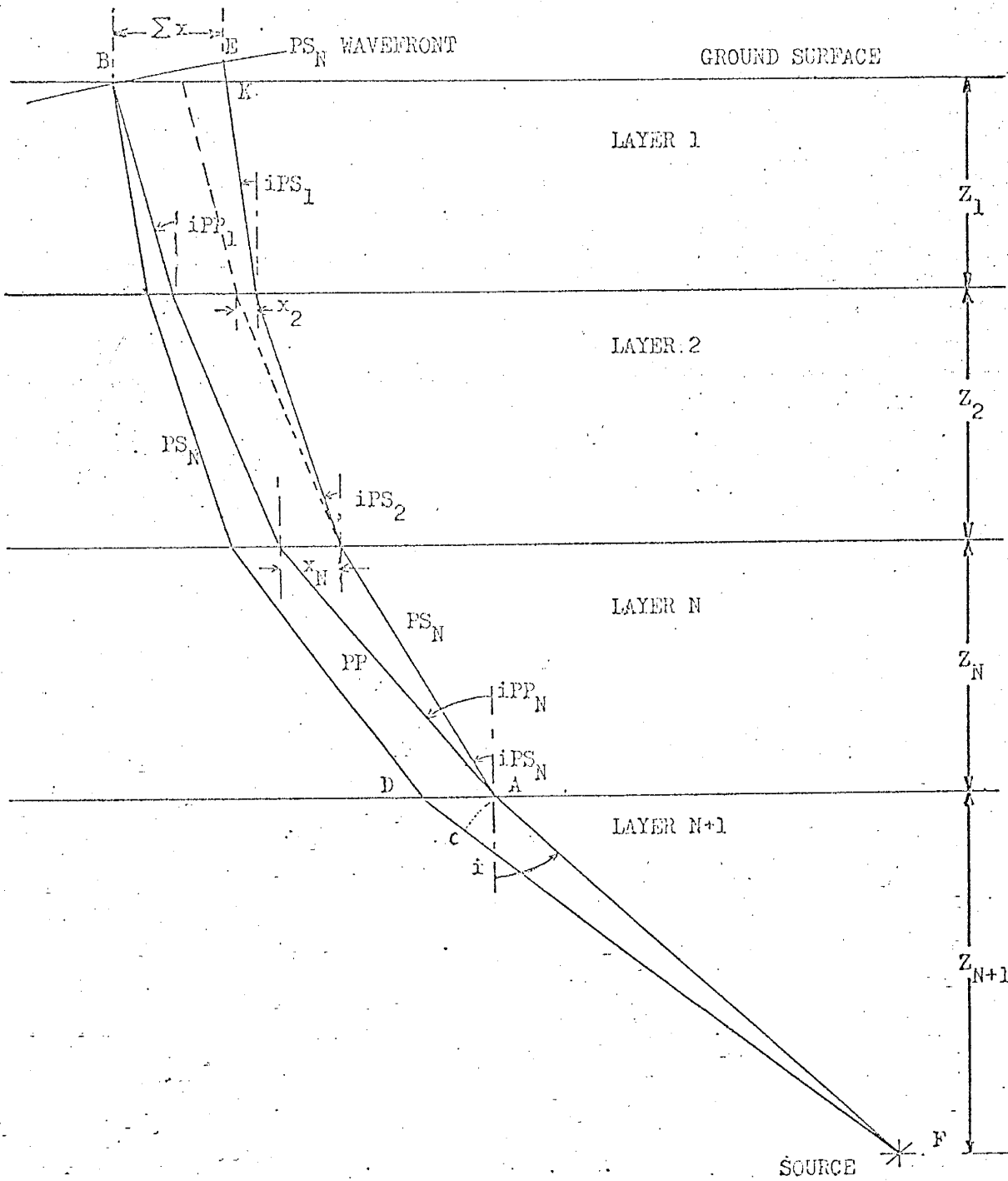$$(PSj-P) = \frac{Zj}{VSj \cdot \cos(iPPj)} - \frac{Zj}{VPj \cdot \cos(iPPj)}$$ (43)

Figure 9. Geometry and nomenclature for P to SV energy conversions in the case of multiple layering.

The total time lag observed on the seismogram due to passage of the waves through the entire section is the sum of the delay times for each individual layer plus a further correction for the additional KE segment of the ray path traversed by the PS_N wave at velocity VS_1.

One form of the approximation leading to equation (5) above is that angle EBK approaches angle iPS_1. Now KE can be given as

$$KE = \sin(iPS_1) \sum_{j=1}^{N} \cdot xj, \qquad (44)$$

where xj is

$$Xj = Zj \left[\tan(iPPj) - \tan(iPSj) \right]. \qquad (45)$$

Substituting equation (45) into equation (44), the additional correction factor for the KE segment is given as

$$\frac{KE}{VS_1} = \frac{\sin(iPS_1)}{VS_1} \cdot \sum_{j=1}^{N} Zj \left[\tan(iPPj) - \tan(iPSj) \right]. \qquad (46)$$

The expression for the total delay (PS_N-P) is given by

$$(PS_N-P) = \sum_{j=1}^{N} \frac{Zj}{VPj} \left[\frac{\sqrt{3}}{\cos(iPSj)} - \frac{1}{\cos(iPPj)} \right] +$$

$$+ \frac{\sqrt{3}\,\sin(iPS_1)}{VP_1} \cdot \sum_{j=1}^{N} Zj \left[\tan(iPP_1) - \tan(iPSj) \right]. \qquad (47)$$

31

Solving (47) for Z_N, obtain equation (48),

$$Z_N = \frac{(PS_N - P) - \sum_{j=1}^{N-1} \frac{Z_j}{VP_j} (A) - \frac{\sqrt{3} \sin(iPS_1)}{VP_1} \sum_{j=1}^{N-1} Z_j (B)}{\frac{1}{VP_N} (C) + \frac{\sqrt{3} \sin(iPS_N)}{VP_1} (D)} \qquad (48)$$

where the various factors are given by

$$A = \frac{\sqrt{3}}{\cos(iPS_j)} - \frac{1}{\cos(iPP_j)} \quad ,$$

$$B = \tan(iPP_j) - \tan(iPS_j) \quad ,$$

$$C = \frac{\sqrt{3}}{\cos(iPS_N)} - \frac{1}{\cos(iPP_N)} \quad ,$$

$$D = \tan(iPP_N) - \tan(iPS_N) \quad .$$

The numberical solution for Z_t, the depth of the base of the Nth interface, must be carried progressively from the surface layer downward. The method is to solve for Z_1 assuming a two layer case using the observed $(PS_1 - P)$ interval. Then using the calculated value of Z_1 from the two-layer case and the observed $(PS_2 - P)$ interval, solve for Z_2 assuming a three-layer case. Continue in a similar manner for successive layers until $N - 1$ layer thickness have been calculated. Upon substitution of the $N - 1$ layer thickness and the $N + 1$ known velocities into equation (47), Z_N is given as a function of i, the angle of incidence of the initial P-wave at the boundary. Then, Z_T, is given by,

$$Z_T = \sum_{j=1}^{N} Z_j. \qquad (49)$$

32

Depth of N-th Interface Based on (S-SP)

The derivation of an expression relating Z_N, the thickness of the Nth layer, to the measured $(S\text{-}SP_N)$ interval is similar to the previous development. Figure 10 shows the geometry and nomenclature for a SP_N converted wave in a section having $N + 1$ layers.

The actual ray path for a SP_N converted wave is FD'B and FAE' is an equivalent time path. The ray path for the refracted SV wave is FAB. The measured $(S\text{-}SP_N)$ interval is the time between the arrival of the converted SP_N wave originating at the base of the n-th layer and the arrival of the refracted SV wave. The time delay due to the passage of the waves through the jth layer is

$$(S\text{-}SP) = \frac{Zj}{VSj\cos(iSSj)} - \frac{Zj}{VPj\cos(iSPj)} \tag{50}$$

The total $(S\text{-}SP_N)$ time lag observed on the seismogram for propagation of the waves from the base of the Nth layer to the detector is the sum of the individual delay times minus a correction term for the K'E' segment of the SP_N ray path traversed by the SP_N wave at velocity VP_1.

Angle E'BK' approaches angle iSP_1 by the approximation leading to equation (16) and the correction term becomes,

$$\frac{K'E'}{VP_1} = \frac{\sin(iSP_1)}{VP_1} \sum_{j=1}^{N} Zj \cdot \left[\tan(iSPj) - \tan(iSSj) \right] , \tag{51}$$

where $Zj \cdot \left[\tan(iSPj) - \tan(iSSj) \right]$ is the distance along the top of the jth layer between the point of incidence of the converted energy ray path and the refracted energy ray path. By adding the correction term to equation (50), using the relationships of Snell's Law and a Poisson's ratio of 0.25
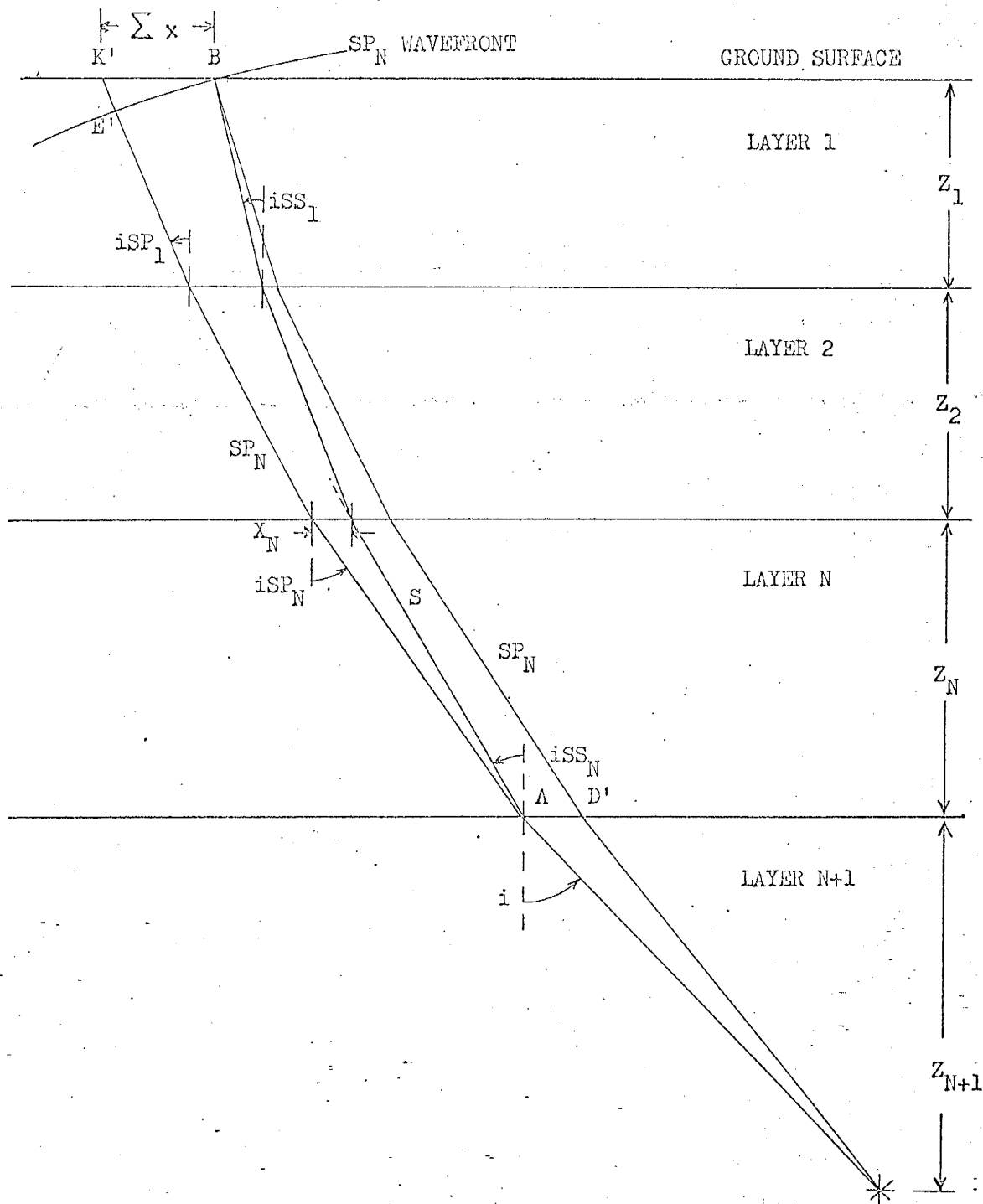
Figure 10. Geometry and nomenclature for SV to P energy conversions in the case of multiple layering.

$$(S\text{-}SP_N) = \sum_{j=1}^{N} \frac{Zj}{VPj} \left[\frac{\sqrt{3}}{\cos(iSSj)} - \frac{1}{\cos(iSPj)} \right] -$$

$$- \frac{\sin(iSP_1)}{VP_1} \sum_{j=1}^{N} Zj \left[\tan(iSP_1) - \tan(iSS_1) \right] . \qquad (52)$$

Solving equation (52) for Z_N , obtain

$$Z_N = \frac{(S\text{-}SP_N) - \sum_{j=1}^{N} \frac{Zj}{VPj} \ (A) + \frac{\sin(iSP_1)}{VP_1} \cdot \sum_{j=1}^{N-1} Zj \ (B)}{\frac{1}{VP_N} \ (C) - \frac{\sin(iSP_1)}{VP_1} \ (D)} , \qquad (53)$$

where the various coefficients are given by

$$A = \frac{\sqrt{3}}{\cos(iSSj)} - \frac{1}{\cos(iSPj)} ,$$

$$B = \tan(iSPj) - \tan(iSSj) ,$$

$$C = \frac{\sqrt{3}}{\cos(iSS_N)} - \frac{1}{\cos(iSP_N)} ,$$

$$D = \tan(iSP_N) - \tan(iSS_N) .$$

The solution for Z_N, the thickness of the nth layer must again be stepwise from the surface layer downward until $N - 1$ thickness and $N + 1$ velocities can be substituted into equation (53) to determine Z_N.

The simultaneous solution of equation (48), which relates the thickness of the Nth layer to observed $(PS_N - P)$ interval and i, the angle of incidence at the base of the Nth layer, and equation (53) which relates Z_N

to the observed $(S - SP_N)$ time lag and also i, gives a unique determination of Z_N. This value may then be substituted into equation (49) to uniquely determine the depth of the base of the Nth layer.

GEOLOGIC SETTING AND LOCATION OF RECORDING STATIONS

A necessary condition for the observation of converted energy phases is that an incident elastic wave encounter an interface with a suitable velocity contrast (see Figure 1). Thick, relatively low speed sedimentary fill materials overlying a normal basinal stratigraphic sequence could furnish such discontinuities. With these criteria as guidelines, three recording sites were selected in the Rio Grande and Snake Ranch structural depressions. The Snake Ranch basin is parallel to and centered 12 miles west of the Rio Grande basin. The occurrence of the two basins is controlled by faulting (Fitzsimmons, 1959). The Socorro Mountain uplift separates the two basins.

The stratigraphy of both depressions is thought to be the same and is generalized in Table 4. The interpretation of a refraction seis-mograph survey conducted in the Rio Grande basin in 1958 indicates that the surface layer consists of at least 1575 feet of 7,000 ft./sec. fill materials. A velocity profile for the remaining sedimentary section was compiled from an assumed distribution of the bulk density of the rocks in the basins. The bulk densities for the stratigraphic column were computed for the interpretation of a gravity survey of the Snake Ranch Flats area (A. R. Sanford, 1968). The compressional wave velocity was derived from the bulk density by means of an empirical relationship based on observations by Rafe and Drake (McCamy et al., 1962). The velocity of the interval from the top of the Precambrian to the micro-earthquake focus was taken to be 20,000 ft./sec. (Sanford and Long, 1965).

The compressional velocity column of Table 4 indicates that the stratigraphic section can be modeled as a five layer case. The amplitude curves of Figure 1 were computed over the range of the assumed velocity distribution of Table 4. The set of curves of the variation in calculated depth values given in Figures 4 through 7 also cover the range of R assumed in Table 4.

Table 4. Generalized geologic column with density and inferred velocity data.

PERIOD	FORMATION	APPROXIMATE THICKNESS (ft.)	BULK DENSITY (gm./cc.)	COMPRESSIONAL VELOCITY (ft./sec.)
QUATERNARY	ALLUVIUM	2,000		7,000
TERTIARY	SANTA FE Gr.			
	DATIL Volc's.	2,500	2.40	
	BACA Fm.	1,000	2.32	
CRETACEOUS	MESAVERDE Gr.	300	2.30	13,000
	MANCOS Sh.	800	2.35	
	DAKOTA Fm.	150	2.41	
TRIASSIC	CHINLE Fm.	350	2.38	
PERMIAN	SAN ANDRES Fm.	400	2.63	15,000
	GLORIETA Ss.	200	2.51	
	YESO Fm.	600	2.53	
	ABO Fm.	500	2.52	
PENNSYLVANIAN	MAGDALENA Gr.	2,150	2.57	
PRECAMBRIAN				20,000

The first recording site, NMT#1, coincides with shotpoint 84 of the 1958 refraction survey. The location is in the Rio Grande depression approximately one mile northwest of the New Mexico Tech Campus (See Figure 11). Two recording stations, SRF#1 and SRF#2 were operated in the Snake Ranch Flats depression. The portable instrument trailer, developed for this project was operated continuously at each station until several microearthquake events of sufficient magnitude and quality for interpretation were recorded. During the field recording, permanent instruments at the New Mexico Tech seismic laboratory, Center Tunnel Site, in the Socorro Mountain uplift were in operation.
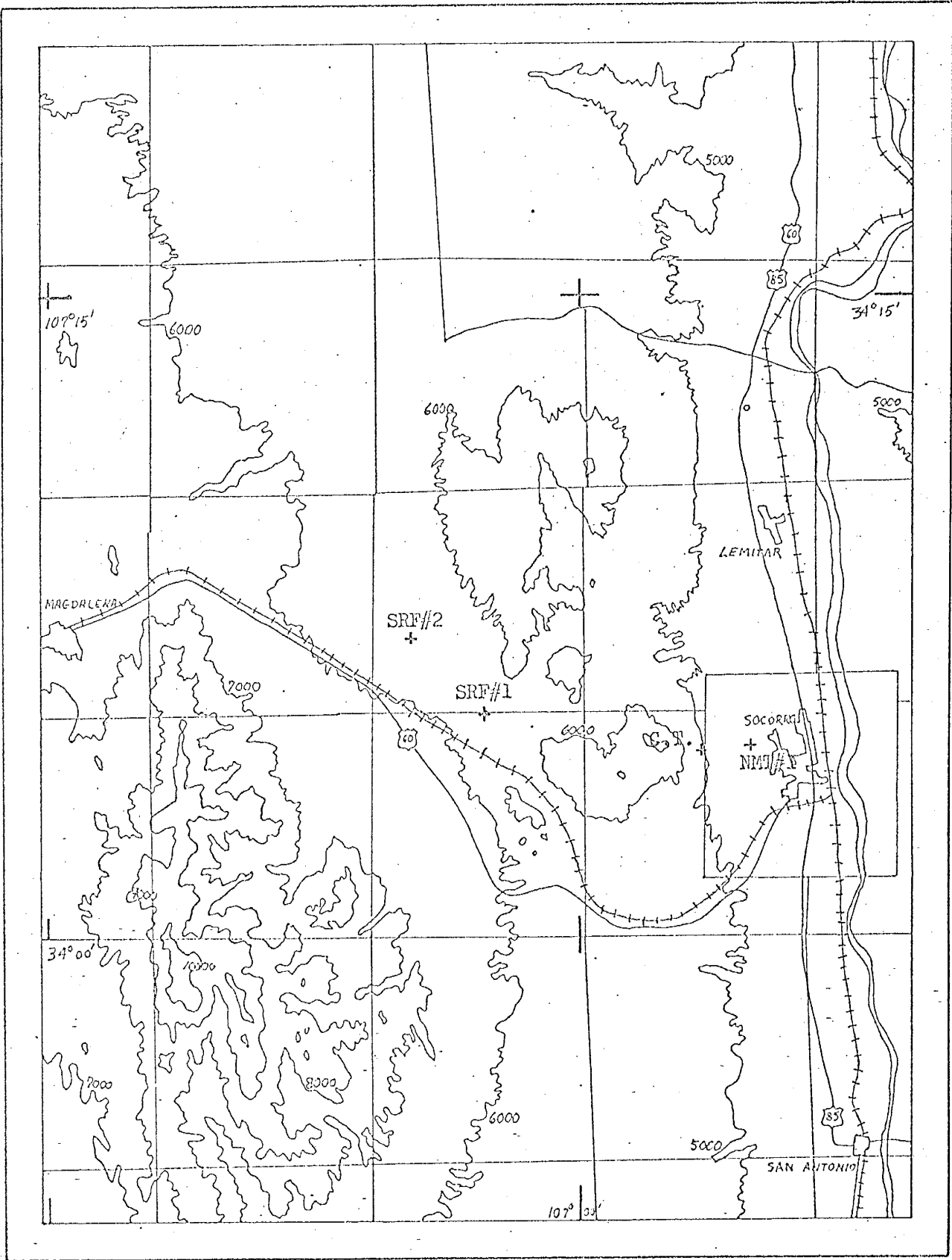
Figure 11.   Location map showing recording stations.

INSTRUMENTATION

Portable and entirely self-sufficient instrumentation was required for remote field recording. A complete set of trailer-mounted equipment was assembled to meet this need. A schematic diagram of the instruments is shown in Figure 10. A 35-watt power requirement was furnished by a thermo-electric generator.

Absolute timing for the system was accomplished through hourly recording of binary coded decimal time signals which are transmitted over WWVB in Fort Collins, Colorado by the National Bureau of Standards. The code was monitored by the 60 khz radio receiver and superimposed directly on the seismic record. Minute marks and hour marks for relative timing reference were generated by means of crystal oscillators in the chronometer-programmer.

A single, vertically-oriented Willmore seismometer was used for the detection of seismic energy arrivals. The movement had a natural frequency of 1.25 Hz and was electrically damped to 0.29 of critical. The seismometer was levelled on a concrete base in the cavity of a vertical chimney tile that was buried about three feet below the ground surface. A protective aluminum plate covered by a mound of earth reduced the input of wind noise into the system.

The actual seismic recording was on 70 mm film. The light beam from a galvanometer which rotates and translates within the recorder is focused on the inside surface of a loop of film wrapped around a transparent drum. By this means, a continuous trace is exposed on the film which, when developed, is very similar in appearance to a conventional drum seismogram (Lehner, 1966). The galvanometer had a natural frequency of 20.4 Hz and was critically damped. The ground motion magnification of the entire system including seismometer, amplifier, galvanometer, and damping is shown in Figure 11. The shape of this curve gives an
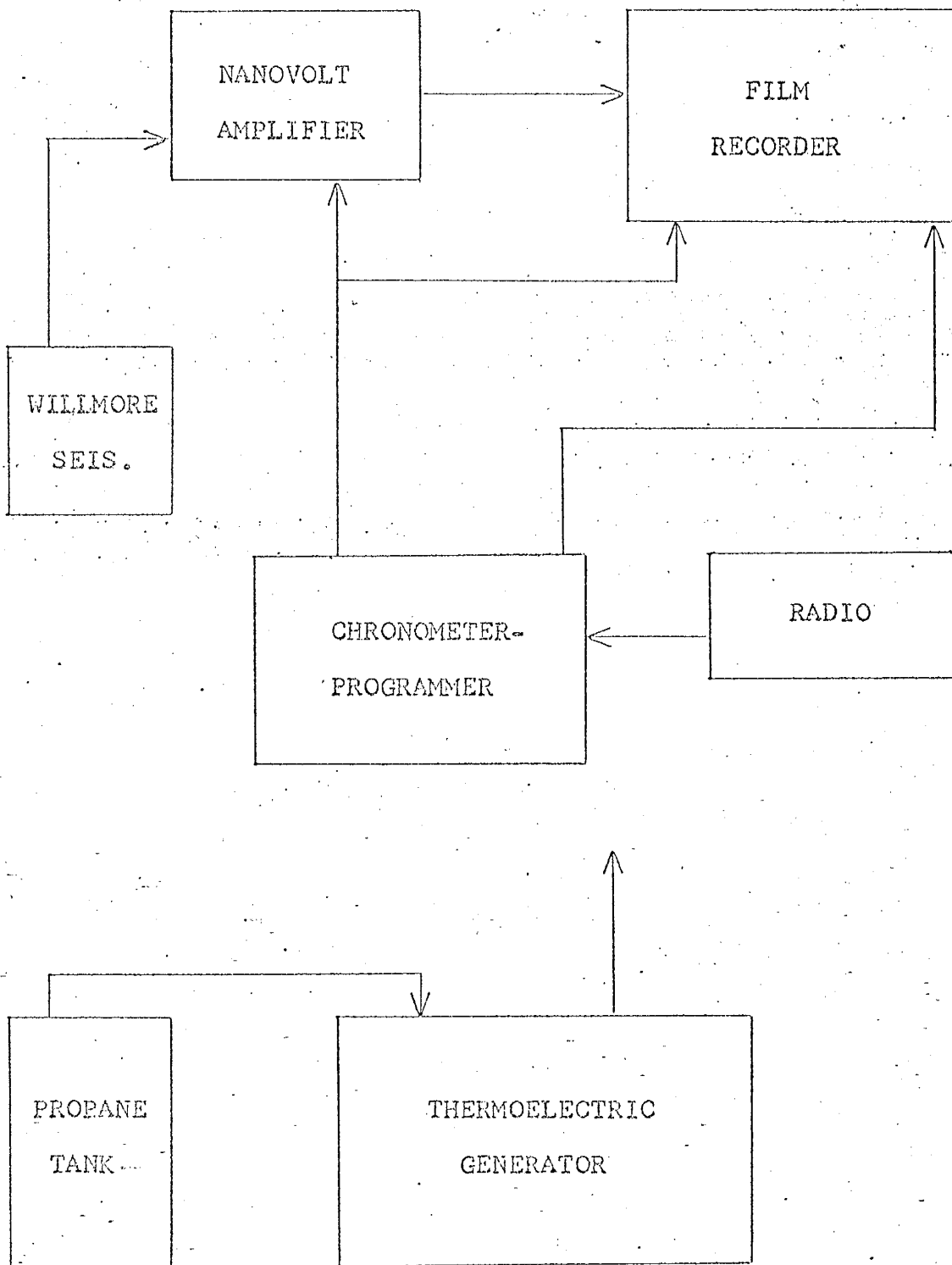
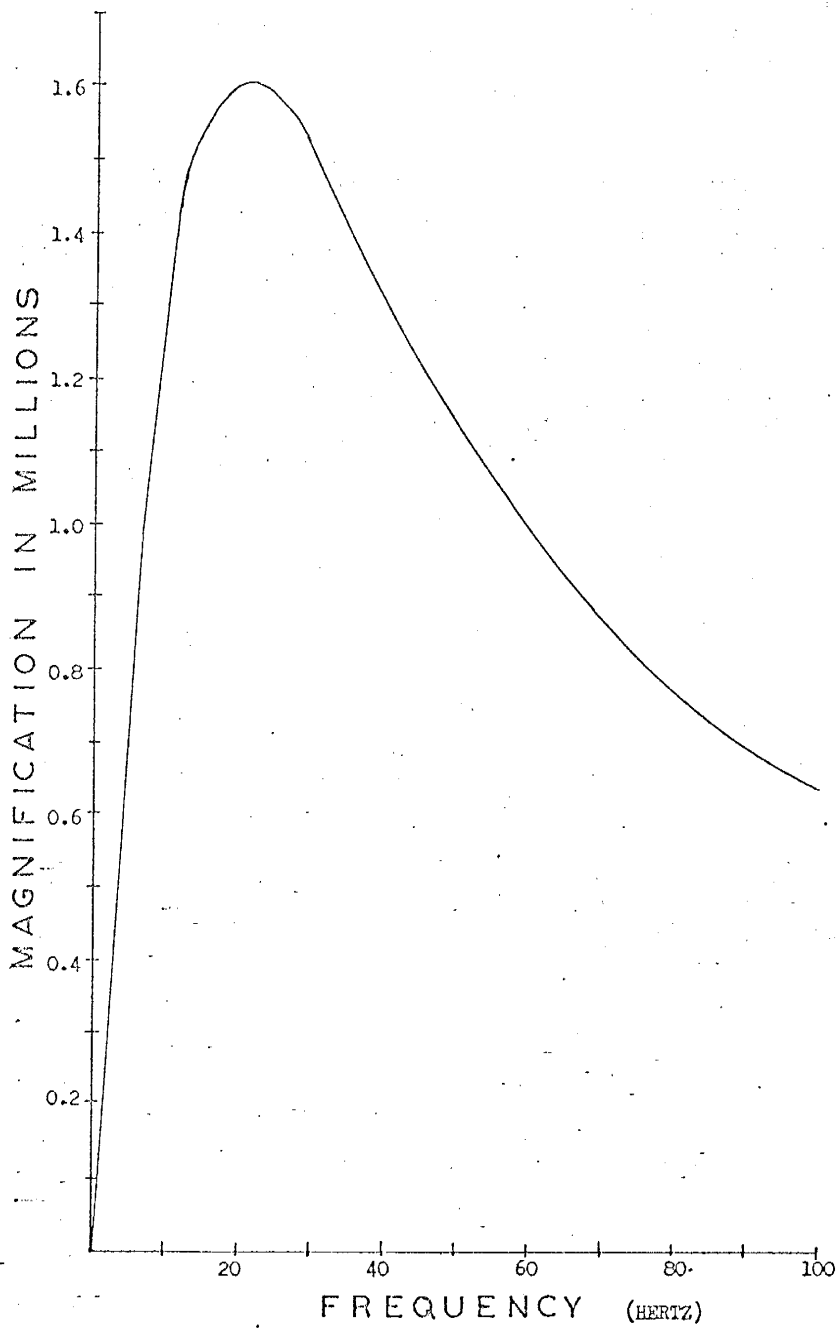Figure 12. Schematic diagram of portable seismograph system.

Figure 13. Amplitude response of trailer mounted seismograph.

DATA PROCESSING

DIGITIZATION

The first step in the preparation of the data was to devise a method of display from which either direct interpretation or digitization and further processing could be carried out. The data was originally recorded at a time scale of four millimeters per second on high-contrast 70 mm film. After development, the film was edited to locate seismic records of interest. Film strips containing events to be analyzed were mounted in a special holder and projected onto a sheet of graph paper by a lantern projector. The events were then traced by hand directly on the paper at a time scale of five inches per second. In many cases, the tracings were sufficiently intelligible to permit direct interpretation. Those tracings which required further enhancement were digitized. The events were digitized directly from the graph paper with amplitude samplings at .025 inch increments which correspond to .005 second time intervals. This sampling rate corresponds to a Nyquist frequency of 100 Hz. Frequencies higher than 100 Hz, should they appear on the tracings, would be aliased by the digitization. However, aliasing did not exist because the field recording system sharply attenuated high frequencies in the neighborhood of the 100 Hz. Nyquist frequency, and the waveform was smoothed by eye to eliminate high frequencies and wind noise as the tracings were produced.

The nature of the tracing method is such that perfect alignment of the arbitrary zero of the graph paper with the rest position of the trace was often difficult resulting in the introduction of a constant amplitude shift and/or a linear trend during the digitization process. As a matter of course, the linear trend was removed from the digitized input data. Each trace was then standardized to a mean value of zero and a standard deviation of one.

45

STACKING

Summing of several microearthquake traces is an effective means of improving the signal to noise power ratio, S/N, by discriminating against random noise interference. The random noise which might be due to wind or digitizing errors is independent of the signal and has the same mean square value of each trace. The signal to noise power ratio of any single seismic trace is given as:

$$S/N = I_s/I_n \qquad (54)$$

where I_s and I_n are respectively the mean square values of the signal and of the noise. The signal to noise power ratio after stacking N seismic traces is (Meyeroff, 1966).

$$S/N = I_s/(1/N)I_n \qquad (55)$$

Amplitude is proportional to the square root of the power and therefore the improvement in the signal to noise amplitude ratio of the resultant traces is expected to be proportional to $\sqrt{N}$.

By visual inspection, two microearthquakes having the same (S-P) interval and frequency content can be inferred to have the same focus on the basis of similiarities in their waveform and character. Energies originating at a common source point and recorded at the same seismometer location will have traversed indentical ray paths. The affects of the transmitting medium on the two traces will therefore be the same and will be enhanced by stacking. Minor misalignment of the two traces will result in a somewhat less than an optimum stack. In this case, the frequency content of the resultant trace will be lowered, and the waveform broadened. This is not too critical in dealing with microearth- quake records of relatively low frequency content.

After digitization, it was possible to determine the best orientation in time of any trace A relative to another trace B, to obtain an optimum stack. This is accomplished through the cross correlation function $R_{AB}(T)$ (Bendat and Piersol, 1966) defined by

$$R_{AB}(T) = \frac{1}{N-T} \sum_{N=1}^{N-T} A_N B_{N+T} \qquad (56)$$

The two traces are best aligned for that value of T at which $R_{AB}(T)$ is maximum. The optimum stack is then obtained after reorientation of the zero time of each event such that $R_{AB}(T)$ is maximum at T = 0.

The previous discussion of the stacking technique is pertinent to the analysis of two or more events generated at a common source. The events to be stacked must be generated by the same type of source mechanism so that the phase of any wave is the same on any record in the ensemble. For example, the P-wave arrival must remain either compressional or dilational throughout the entire suite of records. In addition, the frequency composition of the signal must be similar on each record.

Microearthquakes having different (S-P) intervals but approximately the same angle of incidence can still be stacked in a two-step process. Alignment of the P arrivals and subsequent summing is valid for the enhancement of P and PS phases while alignment of the S arrivals and subsequent stacking may be used to enhance the SP and S phases.

Should the otherwise similar events be sufficiently varied as to location of the source that the angle of incidence at the velocity discontinuity is quite different, than the feasibility of stacking is severely limited. Figure 14 shows the dependence of the (PS-P) time interval upon the

angle of incidence and velocity contrast at a given interface for the case when $VP_1 < VP_2$. The calculations are made for an interface at a depth of 1,000 feet. The ordinate values of the curves correspond to the length of time of the (PS-P) interval at any given angle of incidence as compared to the length of time of that same interval calculated for normal incidence.

The absolute magnitude of time difference is directly proportional to the overburden thickness, Z_1, and inversely proportional to the average overburden velocity VP. To assign real values to the curves, consider P to SV conversions taking place at a velocity interface for which R = 0.5 overlain by 2,000 feet of 10,000 ft./sec. material. The difference between the calculated (PS-P) interval at i = 90° and i = 0° is 0.012 second. In this case, stacking of widely scattered microearthquakes could be used effectively for PS and P enhancement.

The time difference for greater values of R, and for SV to P conversions is considerable larger. The calculated difference between the corresponding (S-SP) intervals in the case cited above is 0.054 second. In this case, stacking could not be used for SP enhancement because the arrivals would be too severely phase shifted between traces. Converted phases generated at sharp velocity reversals cannot be enhanced by stacking because the (PS-P) and (S-SP) intervals differ too widely from trace to trace.

FREQUENCY FILTERING

A general time-domain digital filtering routine was developed for use in data enhancement. The frequency bandpass filters were developed according to discrete Z-transform theory as outlined by Robinson and Treitel (1964). The filter coefficients are derived by taking the Fourier transform of the desired frequency domain response. The filter coefficients are calculated for a resultant filter of the time-delay type.
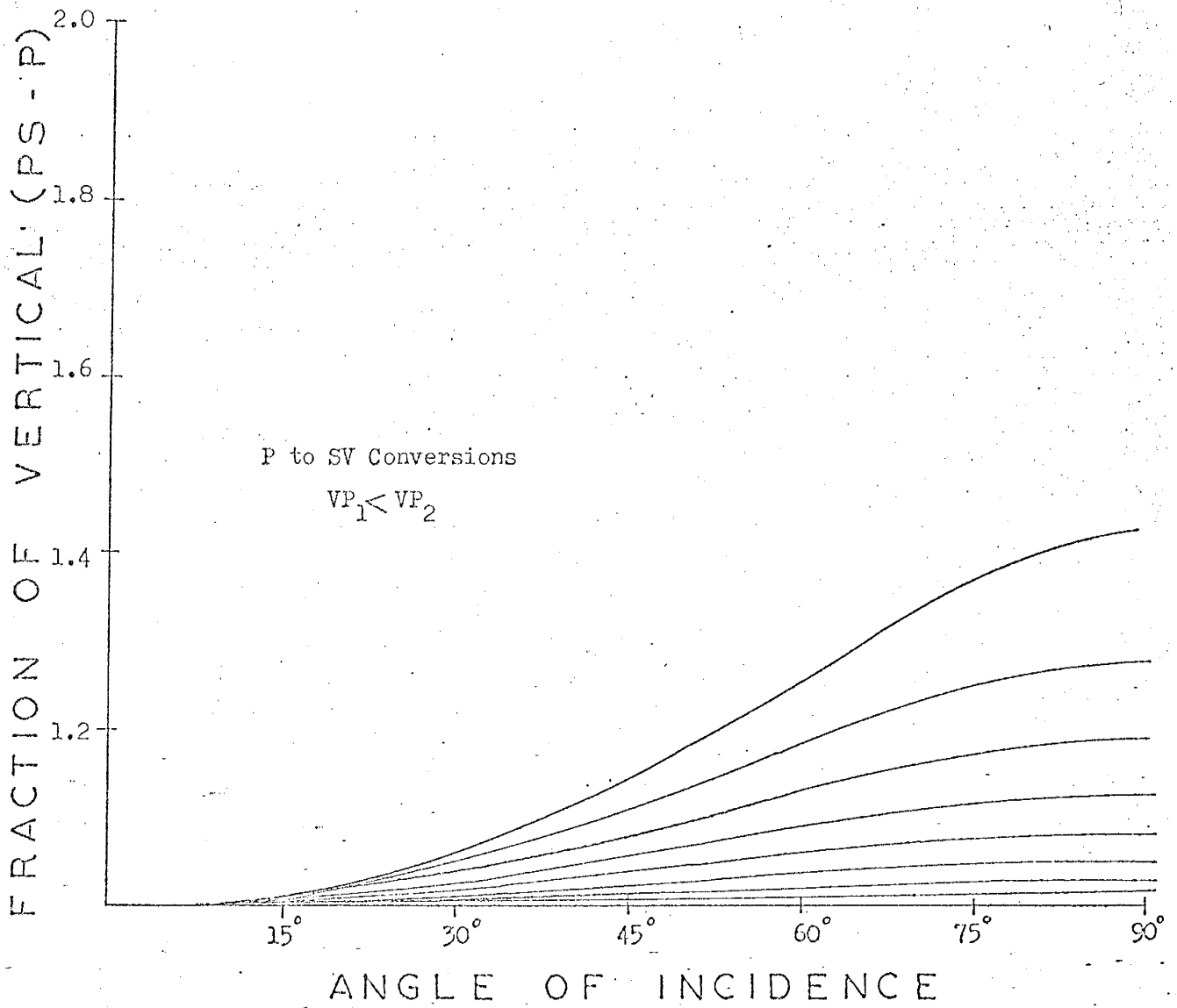
Figure 14. Dependence of observed (PS-P) interval upon i and R for the case where $VP_1 < VP_2$ at an interface of constant depth.

The minimum expected time separation of subsequent arrivals on the raw seismogram is 0.10 second. The time series of filter coefficients was truncated by a Hamming window 21 points wide which corresponds to a maximum delay of 0.10 second. The purpose of the Hamming window is two-fold (Blackman, 1958). The first is to minimize "singing" at the peak frequencies by reducing the effects to the filter's side lobes. The second use is to insure against the superposition of the tails of an early event on the arrival of secondary event. Figure 15 is a plot of the amplitude response and phase lag characteristics of a typical 0 to 10 Hz. low-pass filter which is used in the data analysis. Figure 16 is a plot of the amplitude response and phase lag characteristics of a 10 to 25 Hz. bandpass filter which is also used in the data analysis.

SPECTRAL DENSITY ANALYSIS

The record of each event was analyzed to determine its frequency content. The power spectra density function is obtained by taking the discrete Fourier cosine transform of the autocorrelation function of the trace (Southworth, 1962). The comparison of the power spectra of similar events was used as a criterion for the assumption that the two events had a common source. Spectral analysis was also used as an aid in the choice of filter parameters.
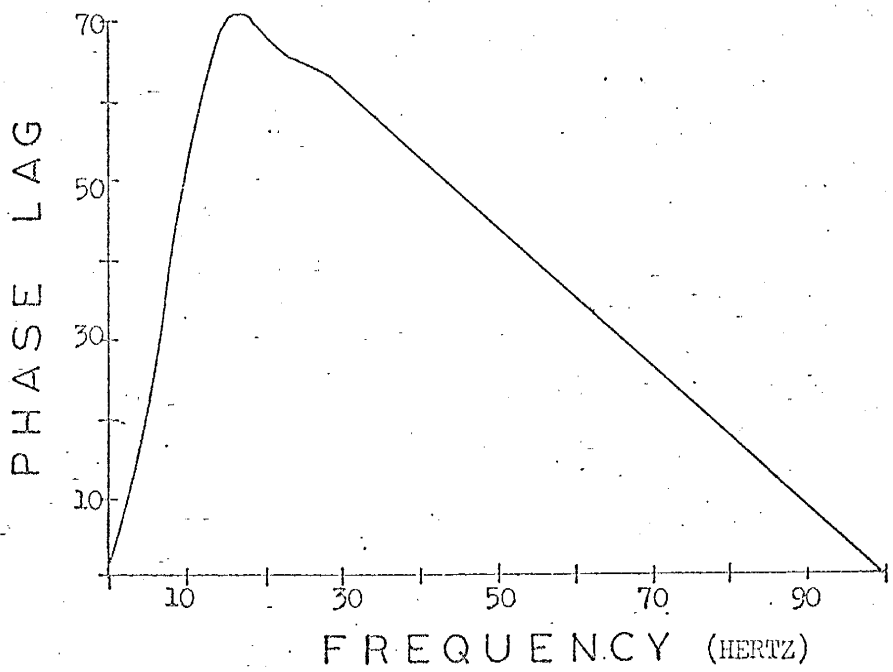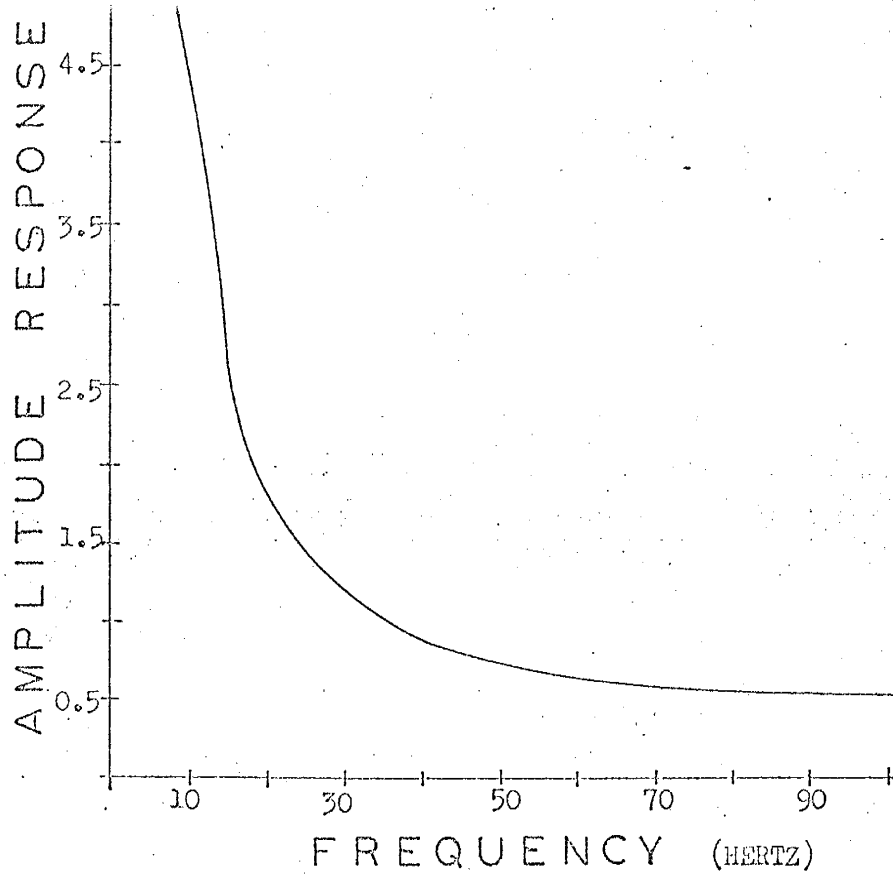
Figure 15. Amplitude response and phase lag characteristics of 0 to 10 Hz. low-pass filter.
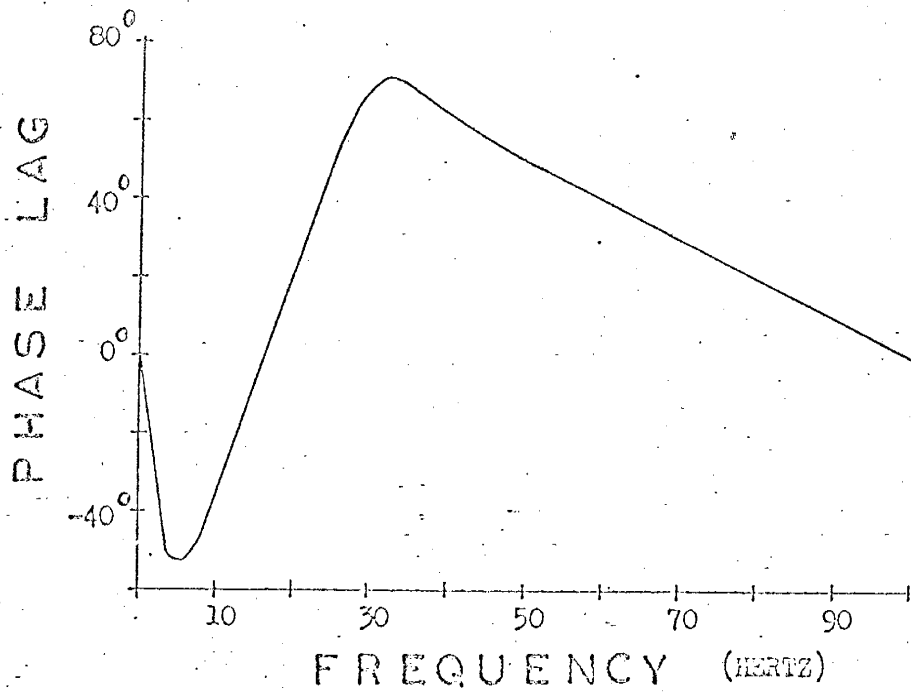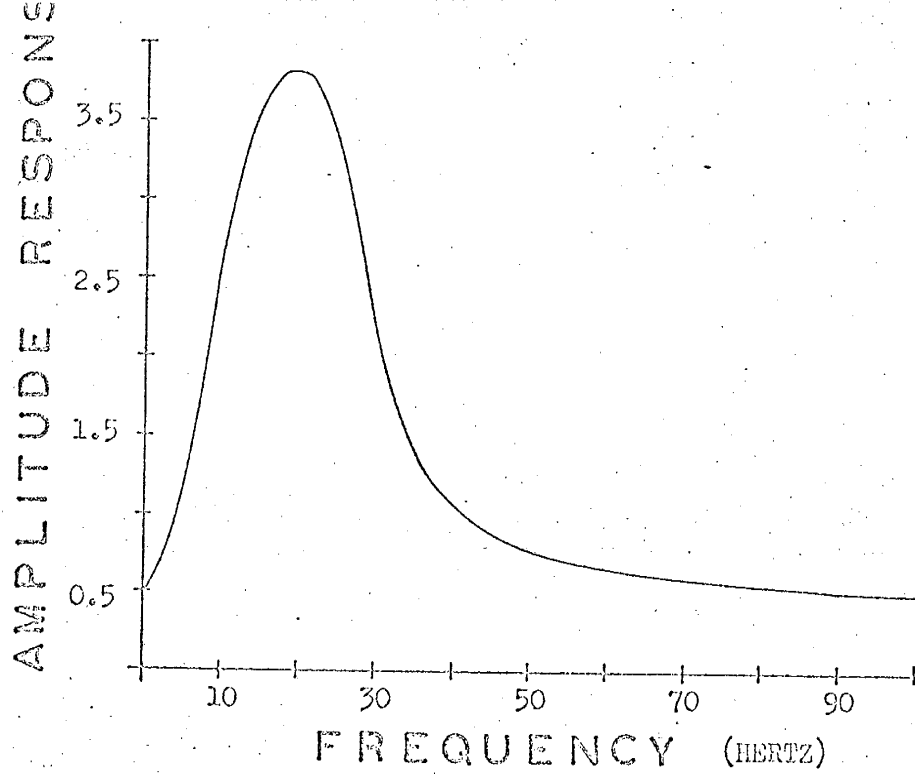
Figure 16. Amplitude response and phase lag characteristics of 10 to 25 Hz. bandpass filter.

PRESENTATION AND DISCUSSION OF DATA

SNAKE RANCH FLATS BASIN

SRF#1 Raw Data And Enhancement

The data recorded at the SRF#1 field station is made up of two groups or swarms of microearthquakes. Group A, the first suite of records, consists of four microearthquakes recorded during the eight-day period from November 2 to November 10, 1967. Figure 17 shows an enlarged segment of the original 70-mm. film strip which contained the event of 10:37, November 10. All four digitized traces, and the trace which is the result of their stacking, are shown in Figure 18 at a normalized amplitude scale.

All records presented in this paper were made with a single vertical-component seismometer. Upward motion on the trace corresponds to upward motion of the ground. The sign of the vertical component of the PS converted wave motion is reversed from that of the direct P wave, and the sign of the vertical component of the SP converted wave motion is reversed from that of the direct S wave (Koefoed, 1962). Therefore the vertical component seismograms will show a phase reversal between the direct and converted waves. The sign of the horizontal components of the PS and SP converted wave amplitudes are identical to the horizontal components of the direct P and S waves.

The total amplitude ratios given in Figure 1 do not take into account single component recording or the free surface effects (Gutenberg, 1964). If both these factors are considered, then for small angles of incidence, the ratio of the vertical components of $\overline{PS}/\overline{P}$ will be significantly smaller than given in Figure 1, and the ratio of the vertical components of $\overline{SP}/\overline{S}$ will be greater than given in
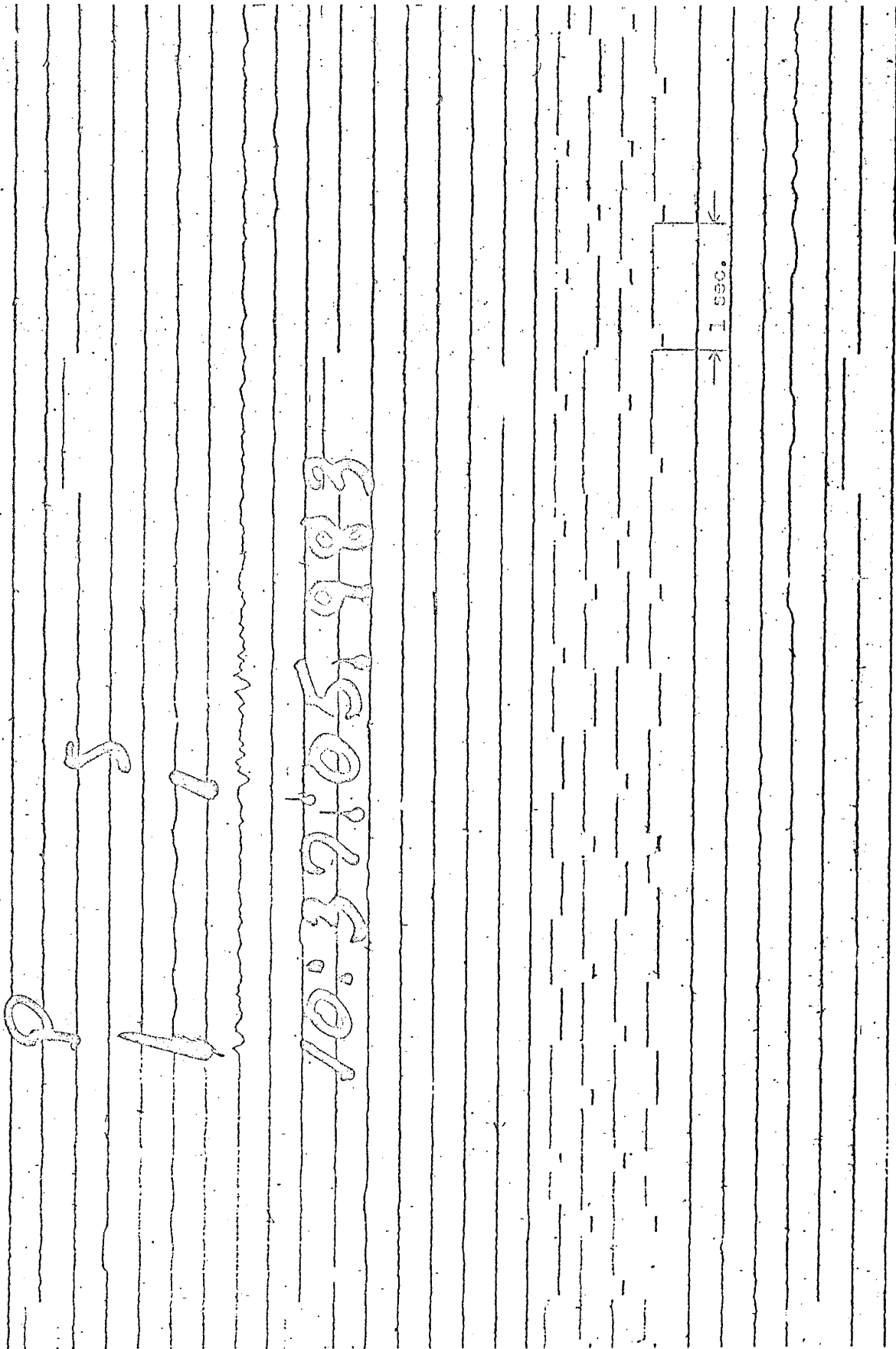
Figure 17. Enlarged segment of the original 70-mm. film recording of the microearthquake of 10:37 November 10, 1967.
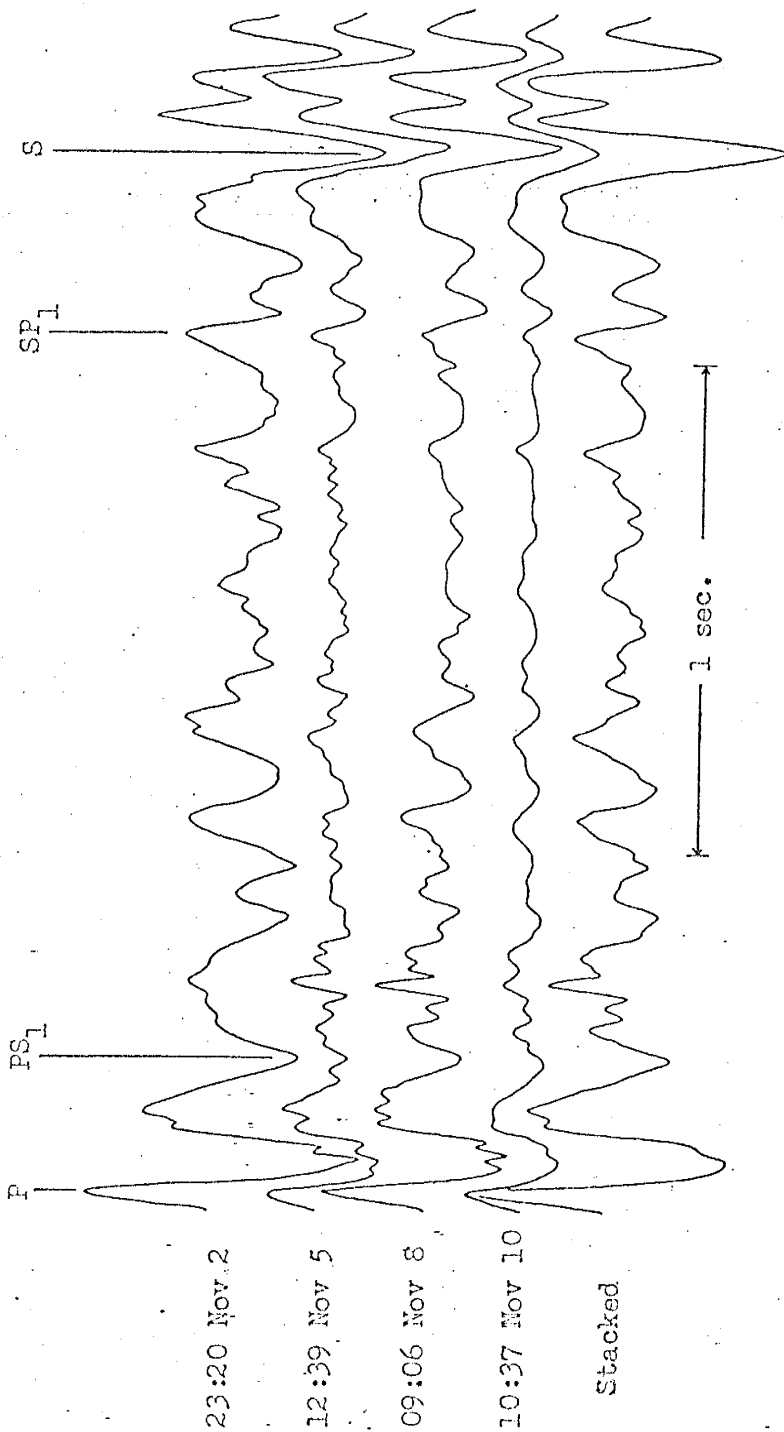
Figure 18. Digitized microearthquake traces of Group A recorded at the SRF#1 station and the result of their stacking. Amplitude scales are normalized.

55

Figure 1. On the other hand, the horizontal components of PS converted phases arriving at the surface at nearly normal incidence, could be expected to have greater amplitudes than the vertical component. Similarly, SP converted phases could be expected to have greatest amplitudes on a vertical component seismogram. Therefore, for best results, identifications of converted phases should be made by comparing records of all components of ground motion.

The converted energy phases are not well defined on the raw seismograms, but the identification can be improved by data enhancement techniques. On the basis of the similarity of their (S-P) intervals, frequency content, and general character, the four microearthquakes in Group A are assumed to have a common energy source. The energy of each event has traveled essentially the same path from source to detector and therefore stacking is applicable. The stacked trace was used only as an aid in the identification and verification of phase arrivals on the raw seismogram. The critical measurement in the analysis is the relative time delay between two successive phases (eg. S and SP). Direct measurements of time intervals are not made on the stacked trace because the pulse broadening or smearing due to slight alignment errors of individual traces will be on the order of the misalignment which may be a few milliseconds.

A visual comparison of P and S waves recorded during the current study and the results of previous studies of Socorro microearthquakes, (Biles, 1967) indicate that the P-wave and S-wave spectra may partially overlap, with the P-wave spectrum containing a relatively greater amount of high frequency motion than the S-phase. The PS converted waves shown in the data presentation are thought to be formed at velocity discontinuities much closer to the detector than to the source. Thus the PS wave has traveled only a small portion of its total path from source to detector as an SV wave, and a comparatively larger segment

as the original P wave. The SP converted wave, on the other hand, has traveled a longer path as the parent SV wave than as a P wave. Therefore one would qualitatively expect the PS waves to be richer in higher frequencies than the SP waves.

All power spectra presented in this paper were computed for the interval of the microearthquake trace from the direct P arrival to the direct S arrival. Therefore effects of the frequency content of the direct S wave were excluded. The power spectra were used as a guide to the design of digital filters. Although the spectrum of PS energy and the spectrum of SP energy probably overlap, the high frequency portion of the spectra is thought to be dominated by the direct P and the PS converted phases, whereas the low frequency portion is thought to be dominated by SP converted energy and other phases (perhaps P to Rayleigh wave conversions). The average of the individual power spectra of the microearthquakes of Group A recorded at SRF#1 is shown in Figure 19.

In Figure 20, the four events of Group A recorded at SRF#1 have been filtered with a 0-10 Hz. low-pass frequency filter. The apparent SP_1 converted energy arrival in the latter half of the record has been enhanced. Figure 15 indicates, that if the S and SP waves are of similar frequency, as they must be in order for both of be enhanced by the narrow bandwidth filter, then they will undergo similar phase shifts during the filtering process. Therefore the time increments between individual SP arrivals can be measured on the filtered version, but the $(S-SP_1)$ interval must still be measured on the raw trace.

In order to enhance the higher frequency components of the possible PS arrivals, each trace was filtered with a 10 to 30 Hz. digital bandpass filter. The filtered traces are shown in Figure 21. The tentatively identified PS converted phase in Figure 21 is significantly enhanced
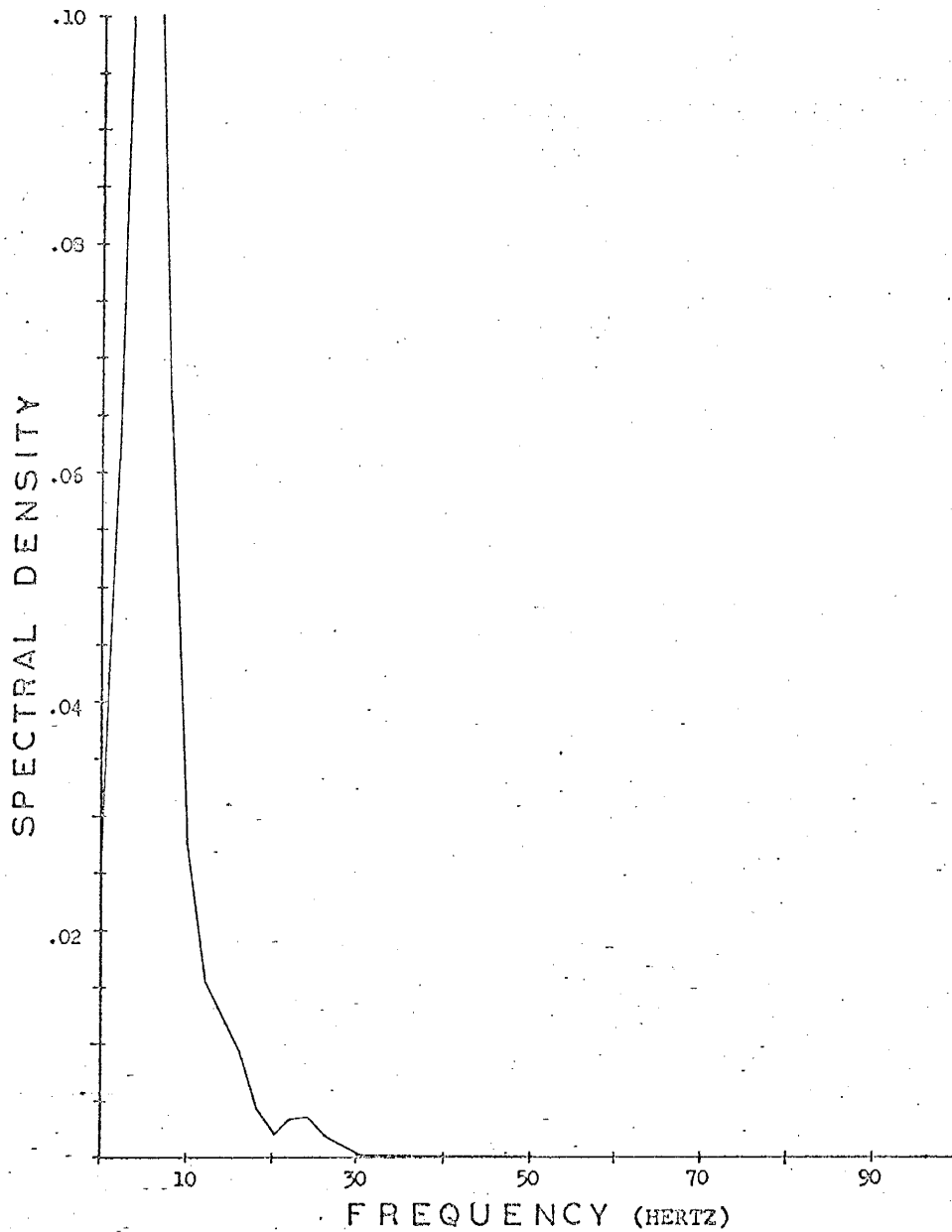
Figure 19. Average of the individual power spectra of the four microearthquakes of Group A recorded at the SRF#1 station.
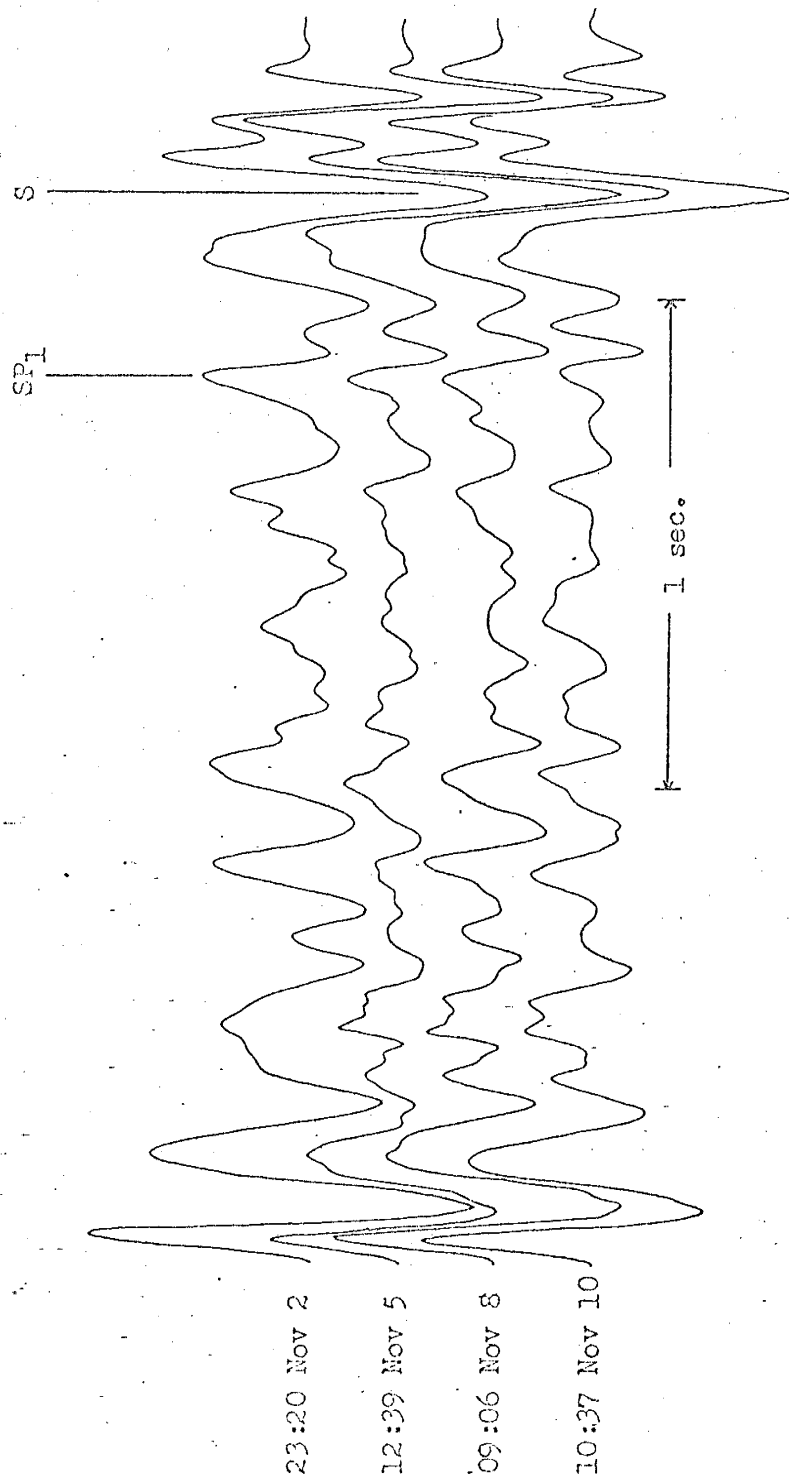
Figure 20. Microearthquake traces of Group A, SRF#1, filtered with 0-10 Hz. digital low pass filter.
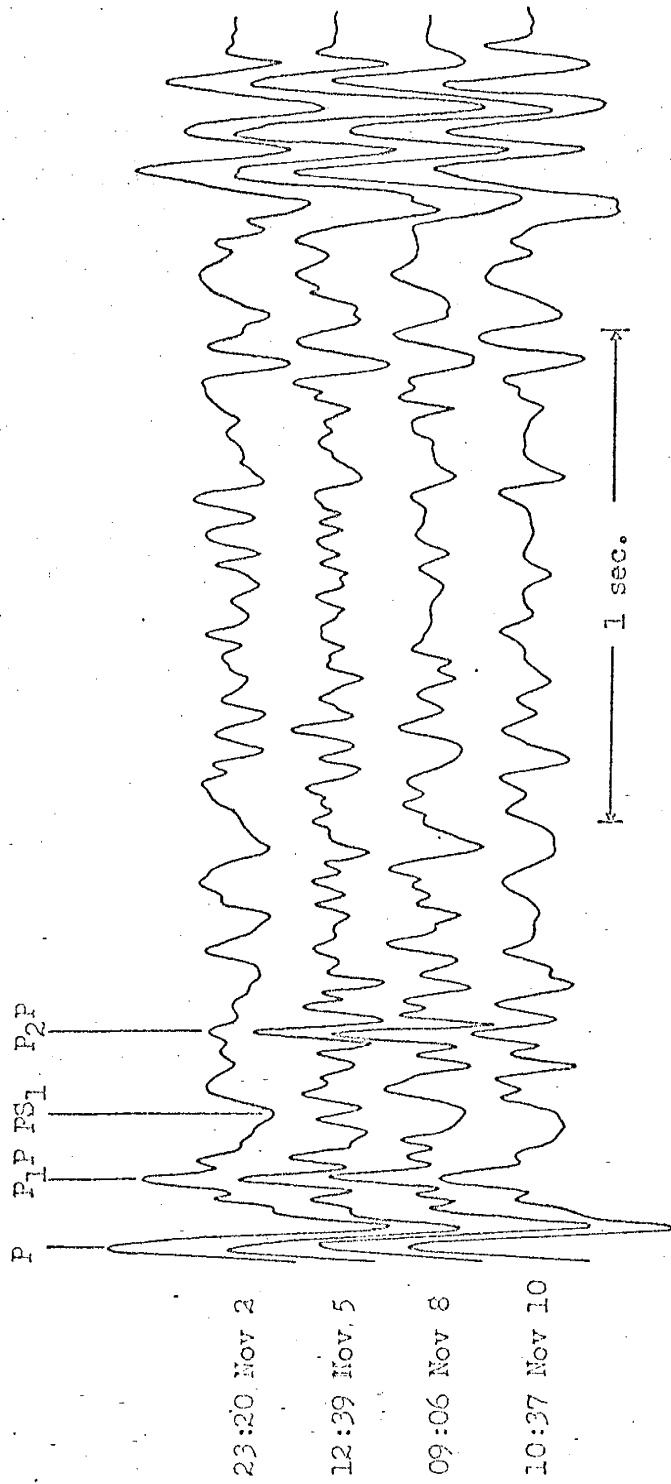
Figure 21. Microearthquake traces of Group A, SRF#1, filtered with 10-30 Hz. digital bandpass filter.

in the early segment of the record. All the PS phases will be somewhat phase shifted by the one-sided filter as indicated by the characteristics of a similar filter shown in Figure 16. The amount of the shift is about the same for all phases having similar frequency content. Thus the time intervals between successive PS arrivals, when identified, can be reliably measured directly on the filtered trace. The $(PS_1 - P)$ interval must still be measured on the raw seismogram. However the identification of the PS_1 arrival on the raw trace was facilitated by comparison with the filtered version.

A comparison of the trace of the event of 10:37, November 10 in Figure 17 with Figures 18, 20, and 21 shows the degree to which the original data was enhanced by the subsequent application of data processing techniques.

Group B, the second set of records taken at SRF#1 station, consists of two microearthquakes recorded during a two hour time span on October 5, 1967. The digitized traces and the result of their stacking are shown in Figure 22 at a normalized amplitude scale. The average of the individual power spectra is shown in Figure 23. The result of 0-10 Hz. low-pass frequency filtering to enhance the SP converted energy arrivals is shown in Figure 24, and the result of 10-30 Hz. bandpass filtering to enhance the P and PS converted energy phases is shown in Figure 25.

SRF#1 Interpretation

The energy arrivals which are denoted as P_1P and P_2P in Figure 25 are identified as reflected P waves generated near the focus. This interpretation is based on the observation of late S wave arrivals on the original records which are probably the corresponding S_1S and S_2S phases.
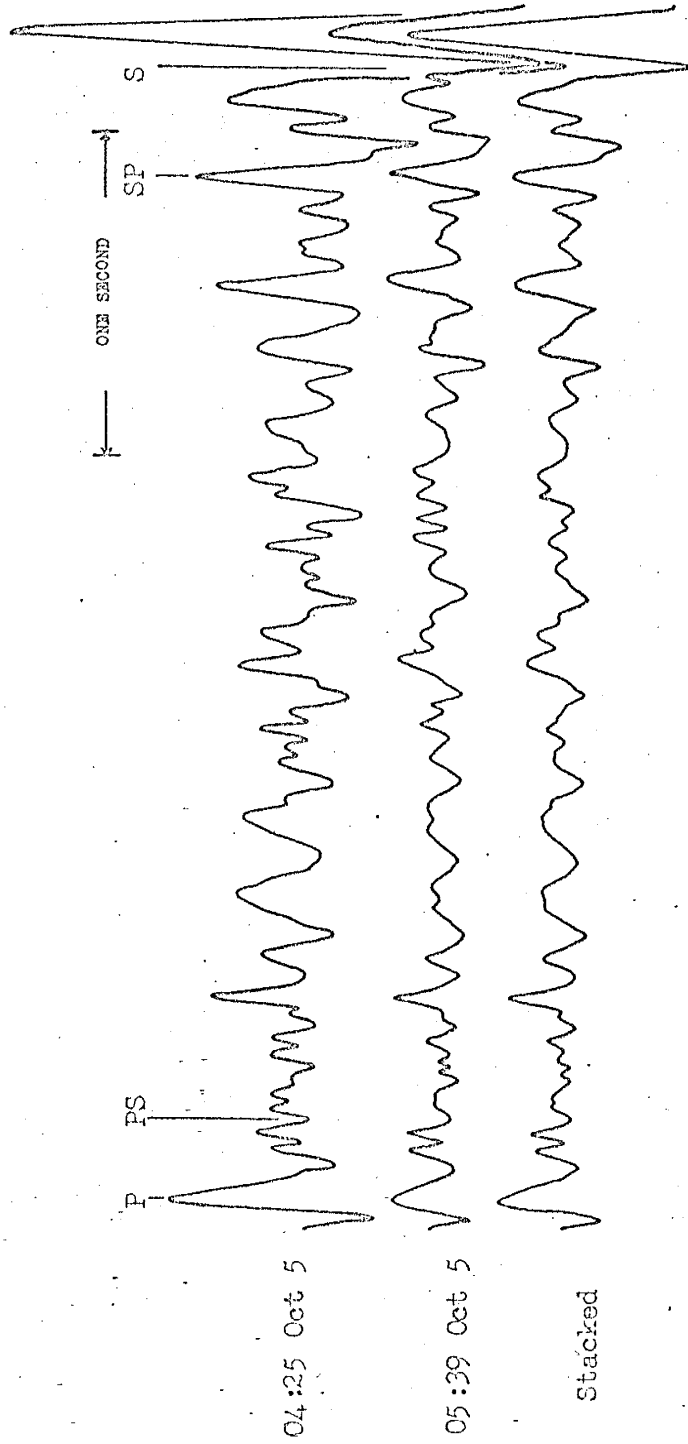
Figure 22. Digitized microearthquake traces of Group B recorded at the SRF#1 station and the result of their stacking. Amplitude scales are normalized.
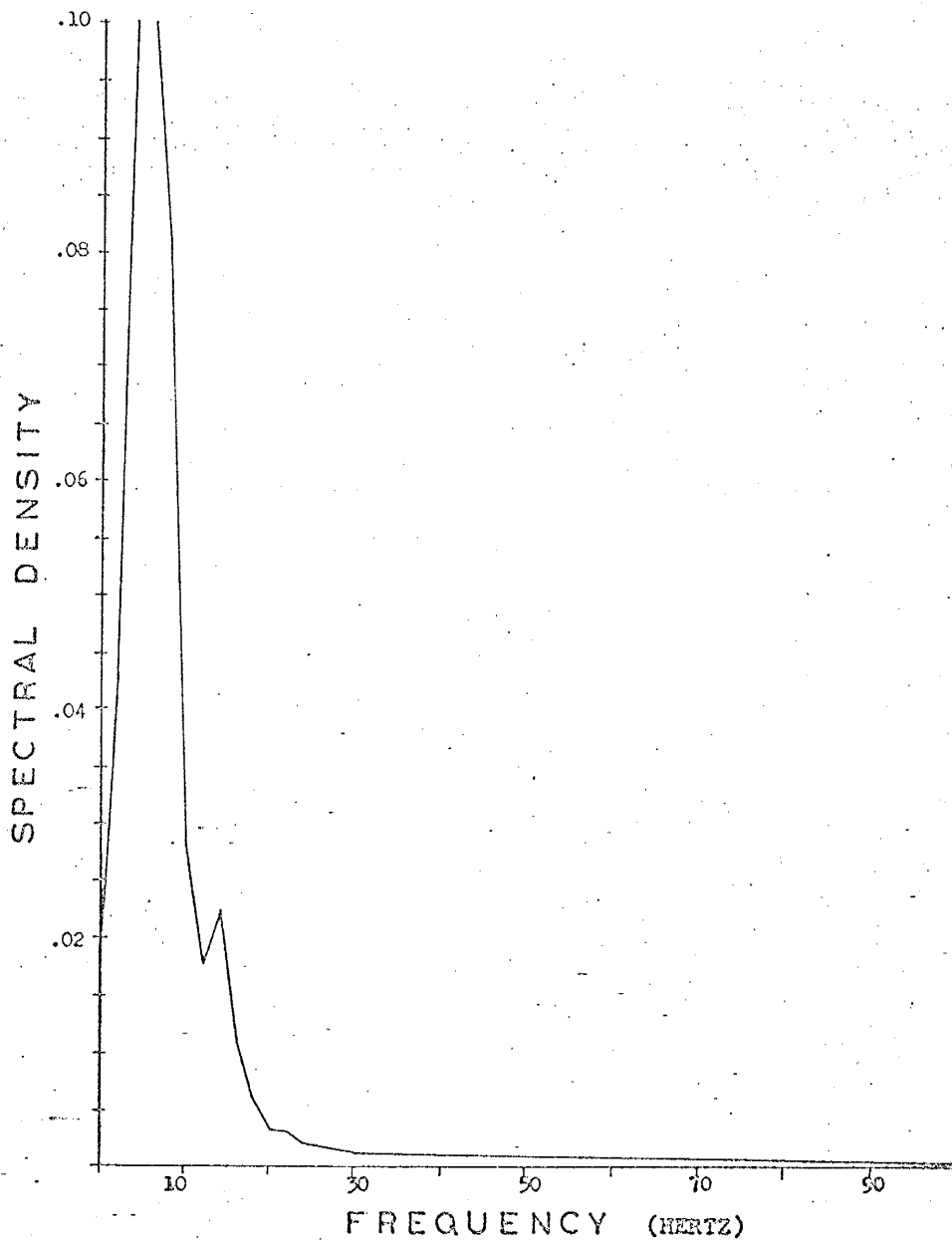
Figure 23. Average of the individual power spectra of the two microearthquakes of Group B recorded at the SNF#1 station.
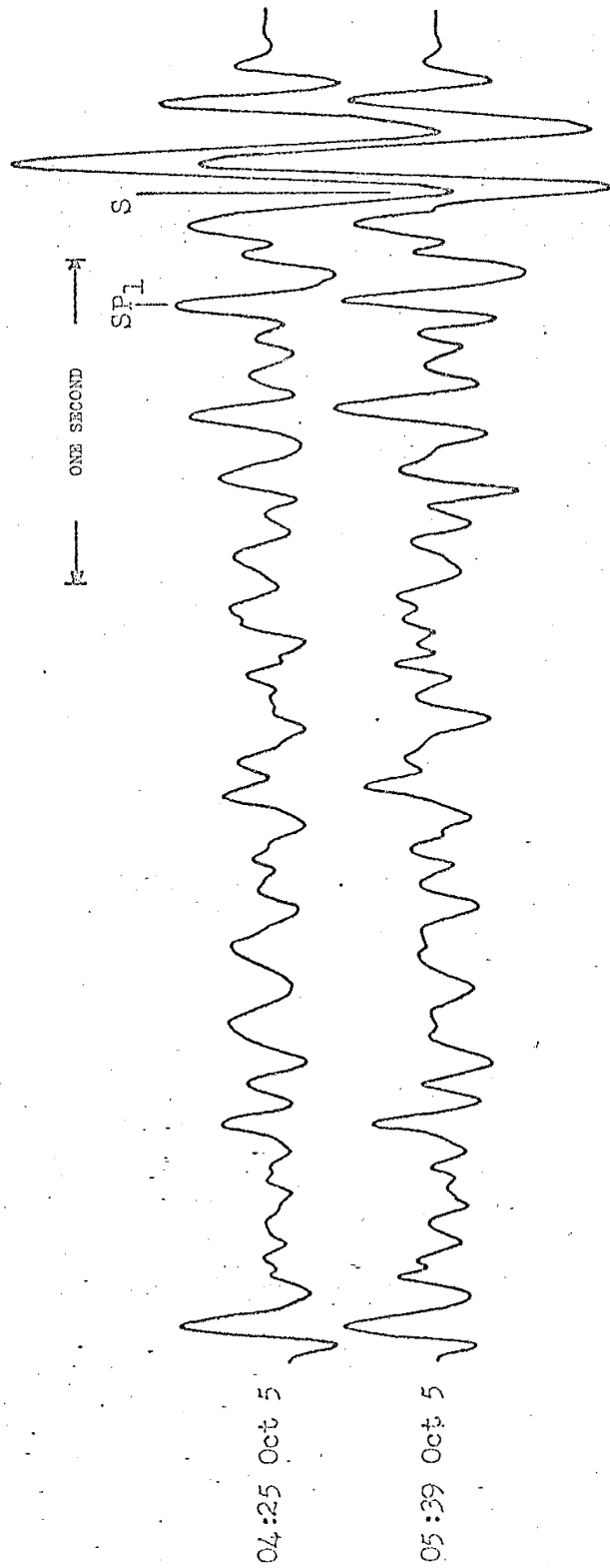
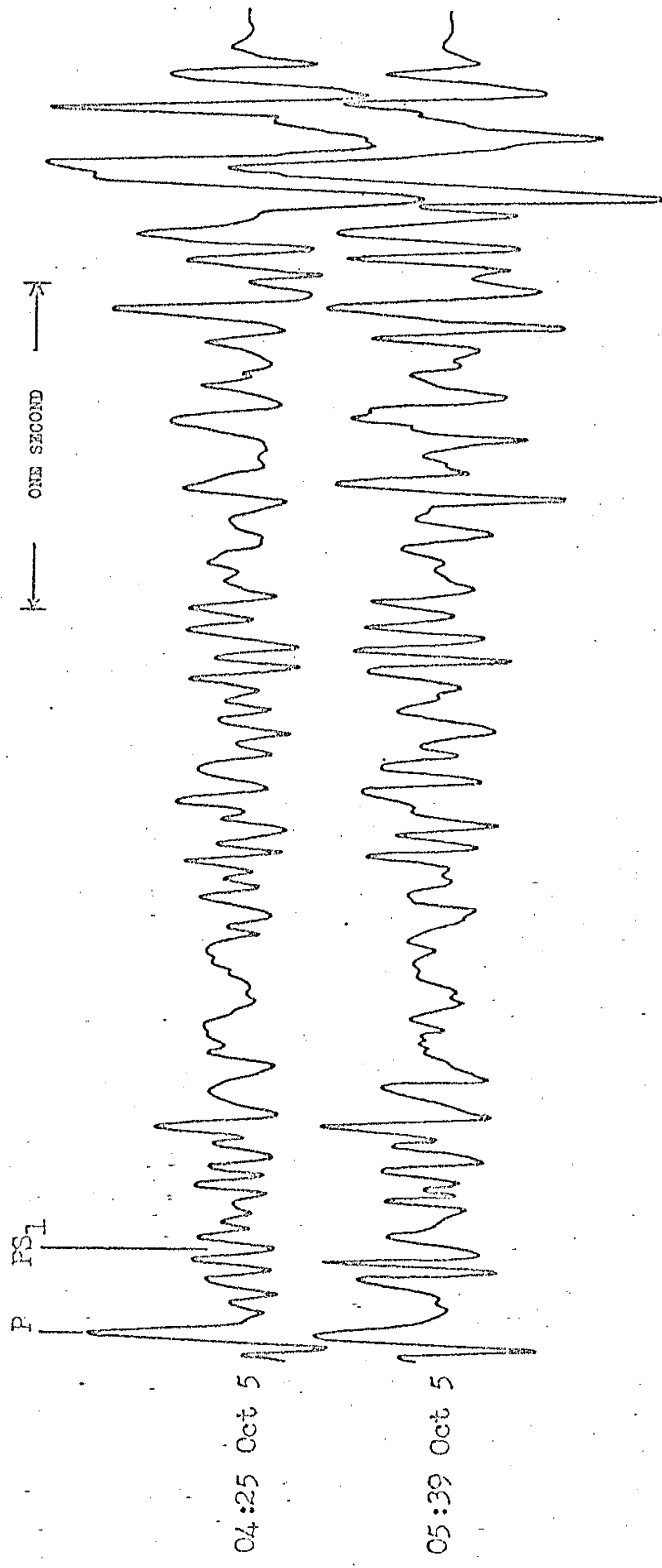Figure 24. Microearthquake traces of Group B, SRF#1, filtered with 0-10 Hz. digital low pass filter.

Figure 25. Microearthquake traces of Group B, SRF#1, filtered with 10—30 Hz. digital bandpass filter.

The interpretation of the series of records taken at the SRF#1 site was carried out on the basis of tentative identifications of the PS_1 and SP_1 converted energy waves, which are assumed to be generated at the interface between the 7,000 ft./sec. layer and the 13,000 ft./sec. layer. This interface has the highest expected velocity contrast in the section according to the assumed velocity distribution of Table 4. The direct P and direct S picks were verified by comparison with simultaneous recordings of the same events made at the permanent Center Tunnel station (see Figure 11).

The calculated depth of the top of the Datil formation (13,000 ft./sec. layer) based on the identification of converted energy arrivals on the records of Group A is 2,500 ft. The corresponding depth calculation from the records of Group B gives a value of 2,300 ft. An average value of 2,400 ft. is taken as the depth of the interface at SRF#1.

The energy source of the microearthquakes of Group A lies at a calculated depth of 20,300 ft. The calculated distance of the epicenter is 37,900 ft. The calculation of the locus of the source of the microearthquakes of Group B places the depth of focus at 16,900 ft. and the radius of the epicenter at 70,300 ft. These are reasonable figures as they are within the range of observed values given for Socorro microearthquakes by Sanford and Long (1965).

The solutions of the equations for the calculation of the depth of focus and distance of the epicenter, equations (40) and (42), do not take into account the possibility of further refractions of the direct waves below 7,000 ft./sec. layer or the dip of the interface. The calculations are based on a straight line path from the source to the base of the 7,000 ft./sec. layer. Any further refractions which are not accounted for would cause the calculated depth of focus to be larger than the true value and the calculated distance of the epicenter to be smaller than the true value. Inasmuch as the values of H and R_c calculated by equations

(40) and (42) are respectively perpendicular to, and parallel to the interface rather than the ground surface, equations (40) and (42) will give misleading results when the interface dips.

The average of the angles of incidence of the direct waves at the surface calculated from the records of Group A is 29°, and the average angle of incidence calculated from the records of Group B is 32°. At these angles of incidence the theoretical vertical component amplitude ratios, $\overline{PS_1}/\overline{P}$ and $\overline{SP_1}/\overline{S}$, are 0.20 and 0.45. The corresponding observed amplitude ratios average 0.33 and 0.39 which is in fair agreement the theory.

The determination of the locations of the energy sources for the microearthquakes of Group A and Group B indicates that the microearthquake foci are widely separated. The observation that the calculated depth of the Datil formation is nearly the same when based on the $(PS_1 - P)$ and $(S - SP_1)$ time intervals from the records produced by two widely separated sources is confirmation that the waves which are identified as PS_1 and SP_1 on the traces must have been generated at a velocity discontinuity within the sedimentary section near the detector rather than near the source.

SRF#2 Raw Data And Enhancement

Three events occurring in a microearthquake swarm on November 19, 1967 were recorded at SRF#2 recording site during a 40-minute time span. The raw records and their stacked sum are shown in Figure 26. The 08:46 and 08:47 events were weak and the initial P motion was not detected. Nevertheless the similarity among the three events throughout the rest of the trace indicates that the energy in each of the three is derived from the same source and has traveled essentially the same path from source to detector.

The average of the individual power spectra of the microearthquakes is shown in Figure 27. A partitioning of the energy content (in the S to P interval of the seismograms) into a low frequency band (below 10 Hz.) and a high frequency band (above 10 Hz.) is indicated.

Figure 28 shows the result of filtering the traces recorded at SRF#2 with a 0-10 Hz. low pass digital filter, and Figure 29 shows the result of filtering with a 10-30 Hz. bandpass filter.

SRF#2 Interpretation

The measurement of the (S-P) interval was made only on the 08:06 trace. Measurements of the $(PS_1 - P)$ and $(S-SP_1)$ time intervals were made on each of the three traces. The $(PS_1 - P)$ interval was taken to be the time between the arrivals of corresponding peaks and troughs of the PS_1 and direct P phases.

The energy source of the November 29 microearthquakes was determined to lie at a depth of 21,200 ft. The distance from the detector to the epicenter was found to be 26,700 ft. These values are within the expected range for Socorro microearthquakes.

On the basis of the picks indicated for the SRF#2 records, the depth of the Datil formation was computed to be 3,500 ft. This is 1,100 ft. deeper than the average value calculated at the SRF#1 site. The distance between stations SRF#1 and SRF#2 is 14,930 ft. The two stations have the same elevation. By migration of the depth data from the two stations, the apparent dip of the Datil formation between the two stations was found to be 4° Northwest.

RIO GRANDE DEPRESSION

NMT#1 Raw Data and Enhancement

On October 27 and 28, 1967, four microearthquakes were recorded at the NMT#1 site. All four events were elements of a microearthquake

swarm which occurred within a time span of 11 hours. The digitized
traces, along with their stacked average, are presented in Figure 30
at a normalized amplitude scale.

The average of the individual power spectra of the traces is
shown in Figure 31. As in the case of data for the SRF#2 site, the
energy is partitioned into a low frequency band (0-10 Hz.) and a
high-frequency band (10-25 Hz.)

The results of low frequency filtering with a low-pass 0-10 Hz.
digital filter are shown in Figure 32. The low-pass filtering was designed
to enhance the SP converted energy phases. Bandpass frequency fil-
tering in the 10-25 Hz. range was applied to the raw data to enhance the
P and possible PS energy arrivals in the early segment of the trace.
The results are shown in Figure 33.

Interpretation (NMT#1)

The interpretation of the series of records taken at the NMT#1
site was carried out on the basis of a fairly reliable identification of
the SP_1 phase and an uncertain identification of the PS_1 phases.
From the measured $(PS_1 - P)$ and $(S - SP_1)$ intervals, the calculated
angle of incidence at the surface, iPP_1, is 20° assuming the converted
waves are developed at a horizontal interface between the 7,000 ft/sec.
layer and the 13,000 ft./sec. layer. The curves of Gutenberg (1944)
and Figure 1 indicate that for this small angle of incidence, the expected
ratio of the vertical component of PS_1 to the vertical comp of P is on
the order of 0.1. Under these assumptions, the PS_1 wavelet should be
too small for positive identification. However if the interface at which
conversion occurs dips eastward, the angle of incidence at the surface
increases. The large observed $\overline{PS_1}/\overline{P}$ amplitude ratio might be ex-
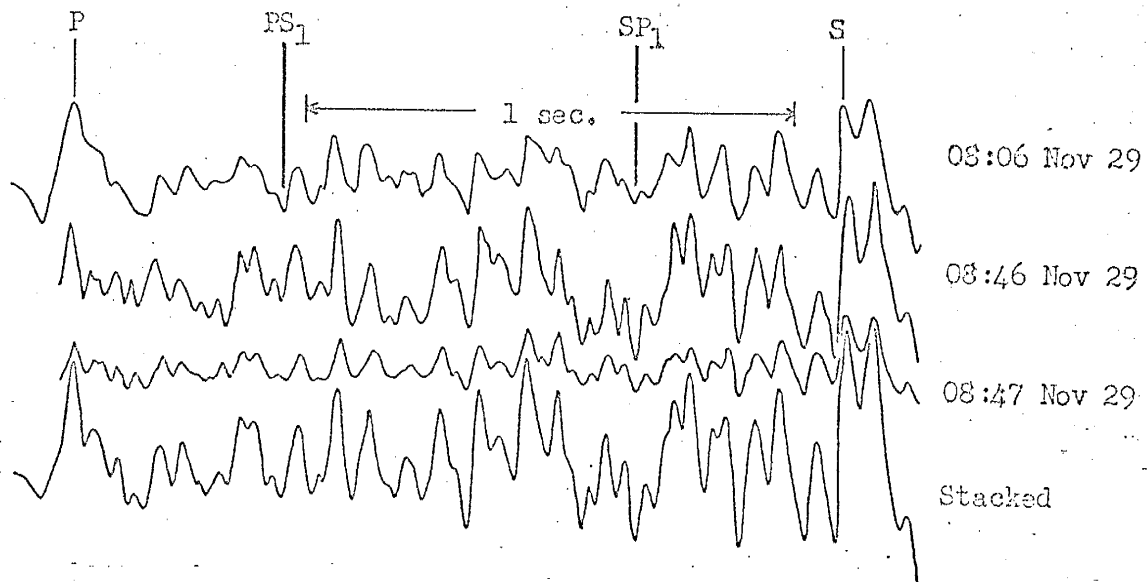plained in this way. Assuming the velocity distribution of Table 4, the

Figure 26. Digitized microearthquake traces recorded at the SRF#2 station and the result of their stacking. Amplitude scales are normalized.
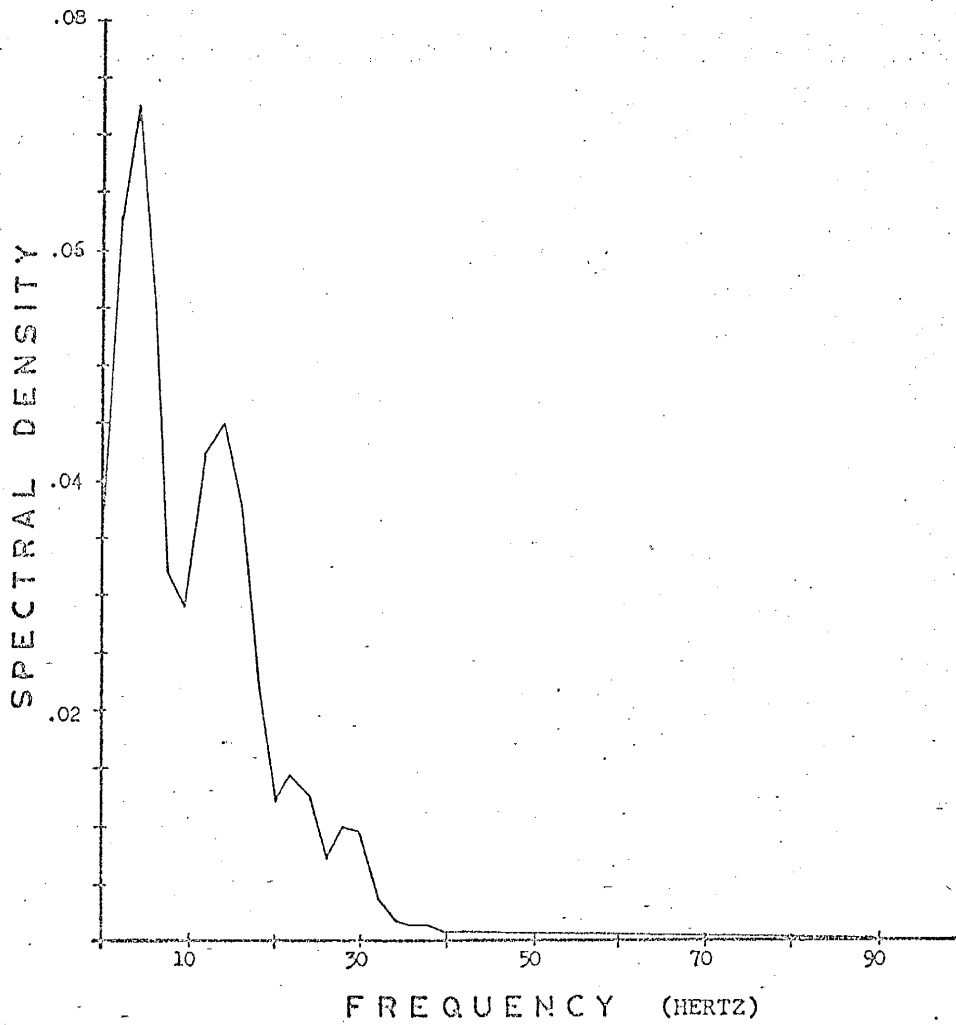
Figure 27. Average of the individual power spectra of the three microearthquakes recorded at the SRF#2 station.
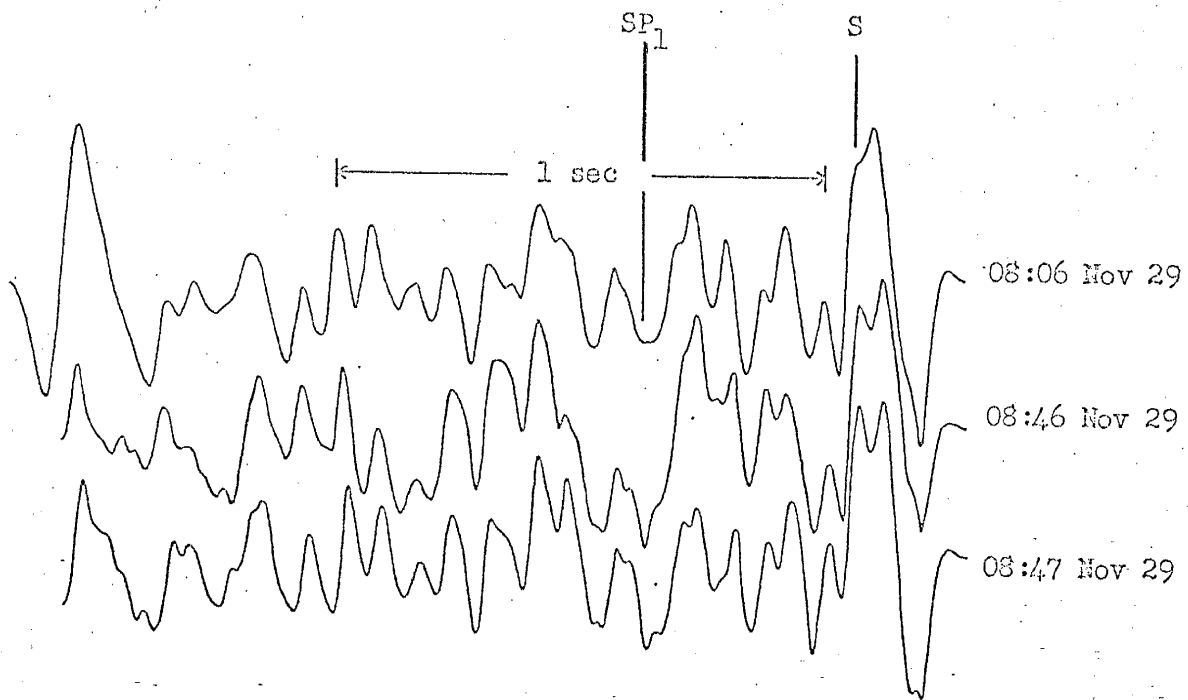
Figure 28. Microearthquake traces recorded at SRF#2 filtered with 0-10 Hz. low pass digital filter.
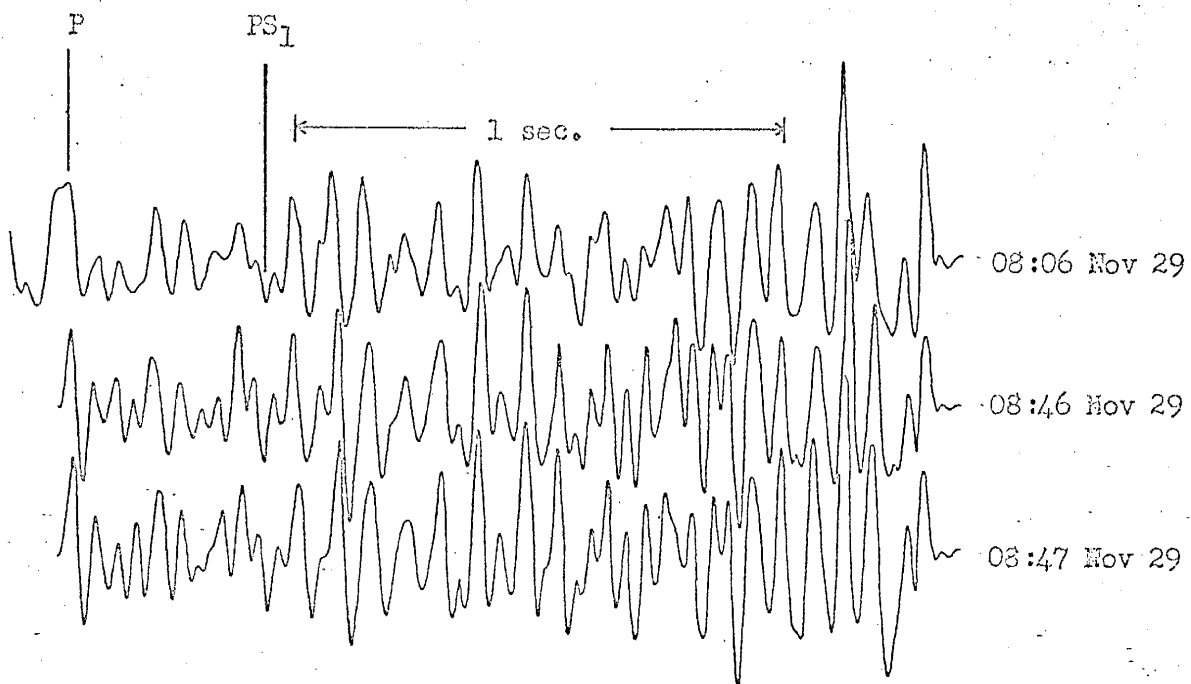
Figure 29. Microearthquake traces recorded at SRF#2 filtered with 10-30 Hz. bandpass digital filter.
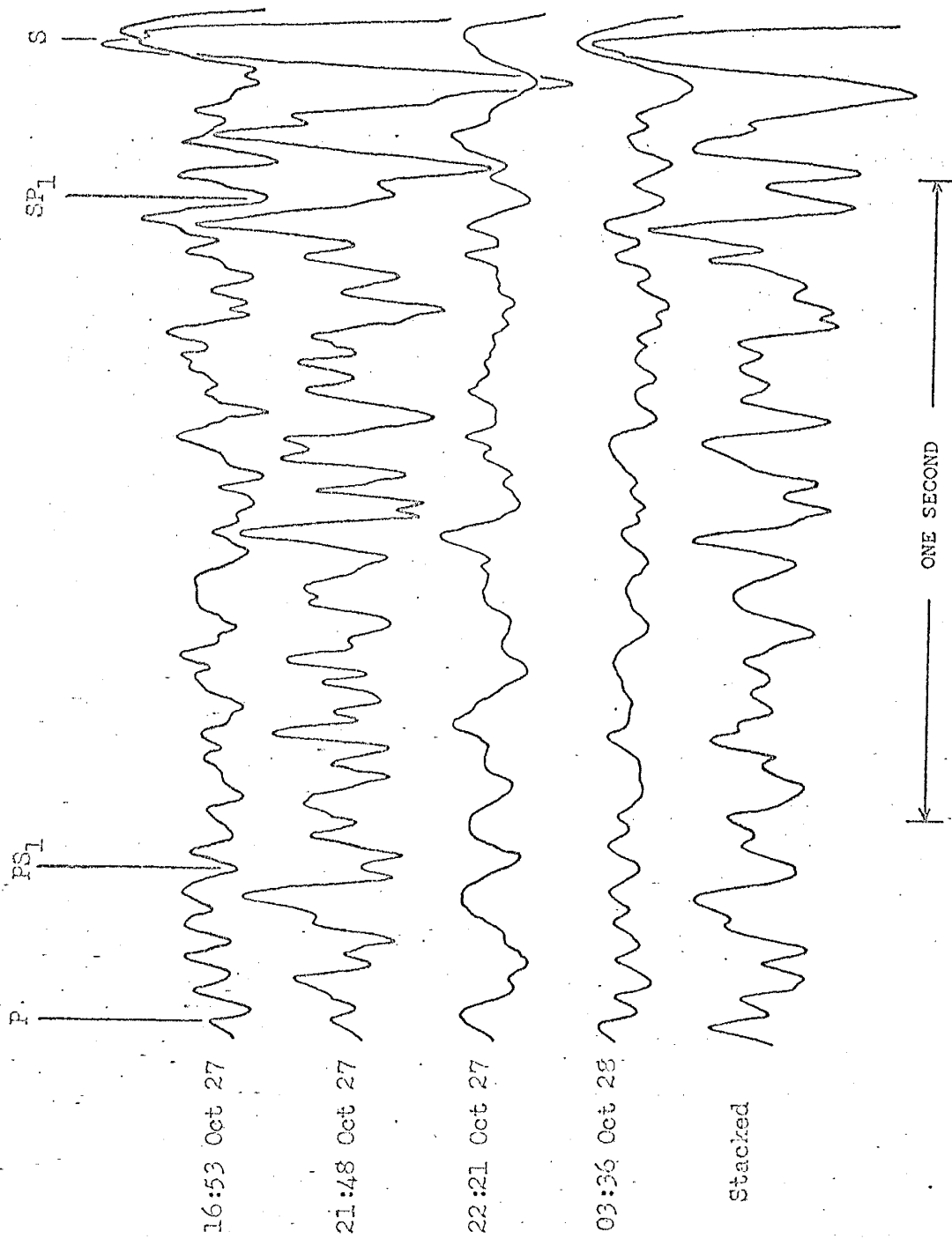
Figure 30. Digitized microearthquake traces recorded at the MNTW station and the result of their stacking. Amplitude scales are normalized.
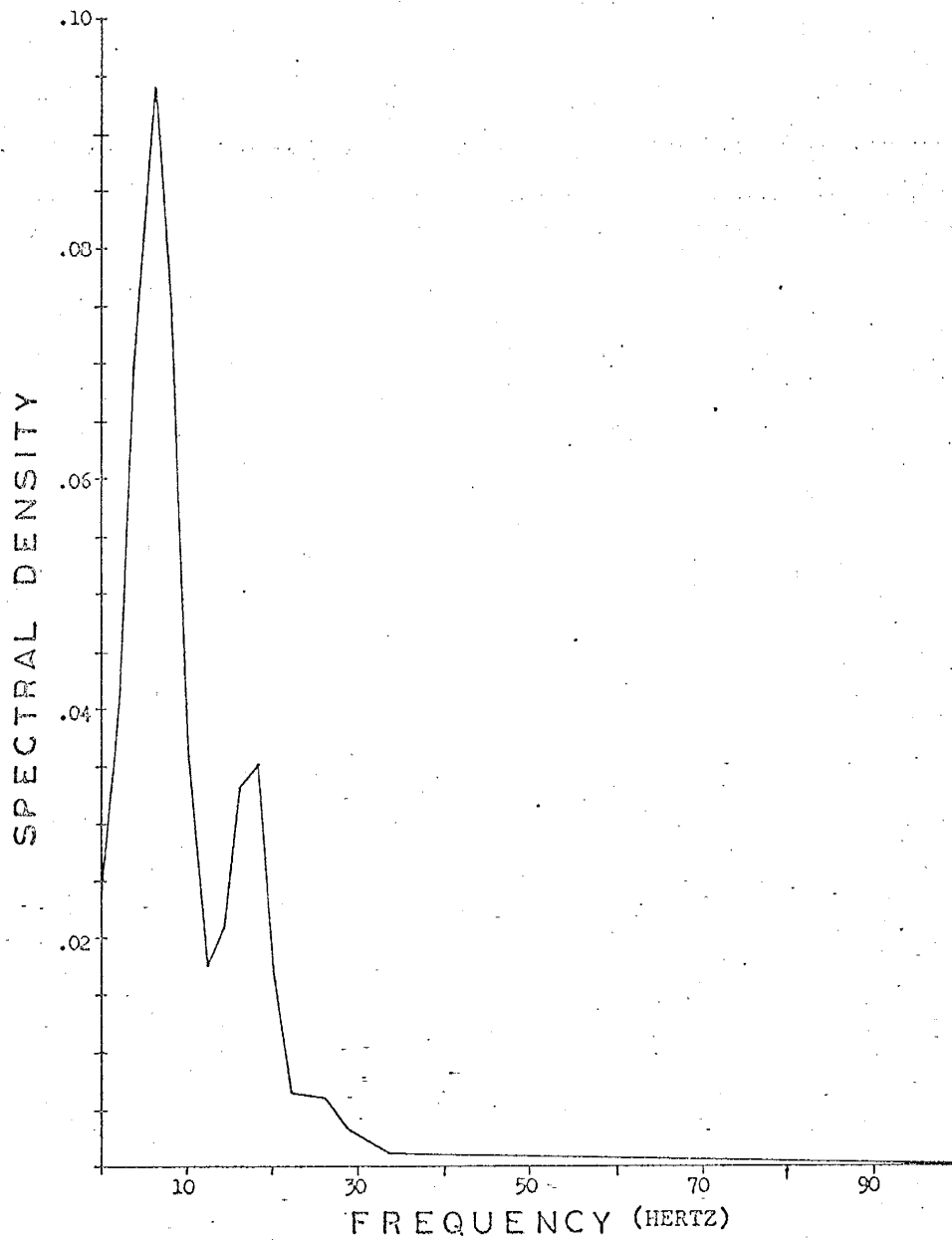
Figure 31. Average of the individual power spectra of the four microearthquakes recorded at the NMT#1 station.
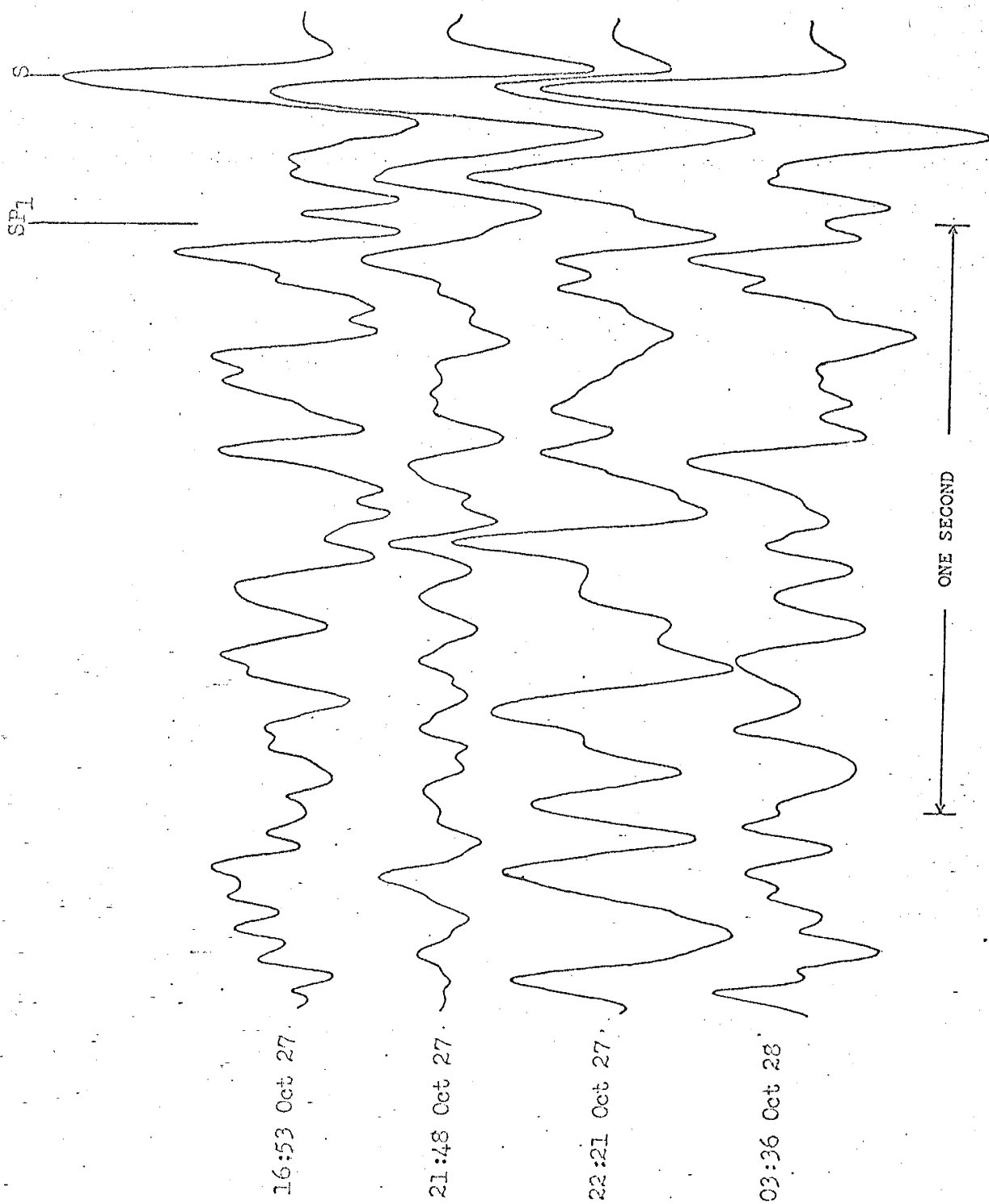
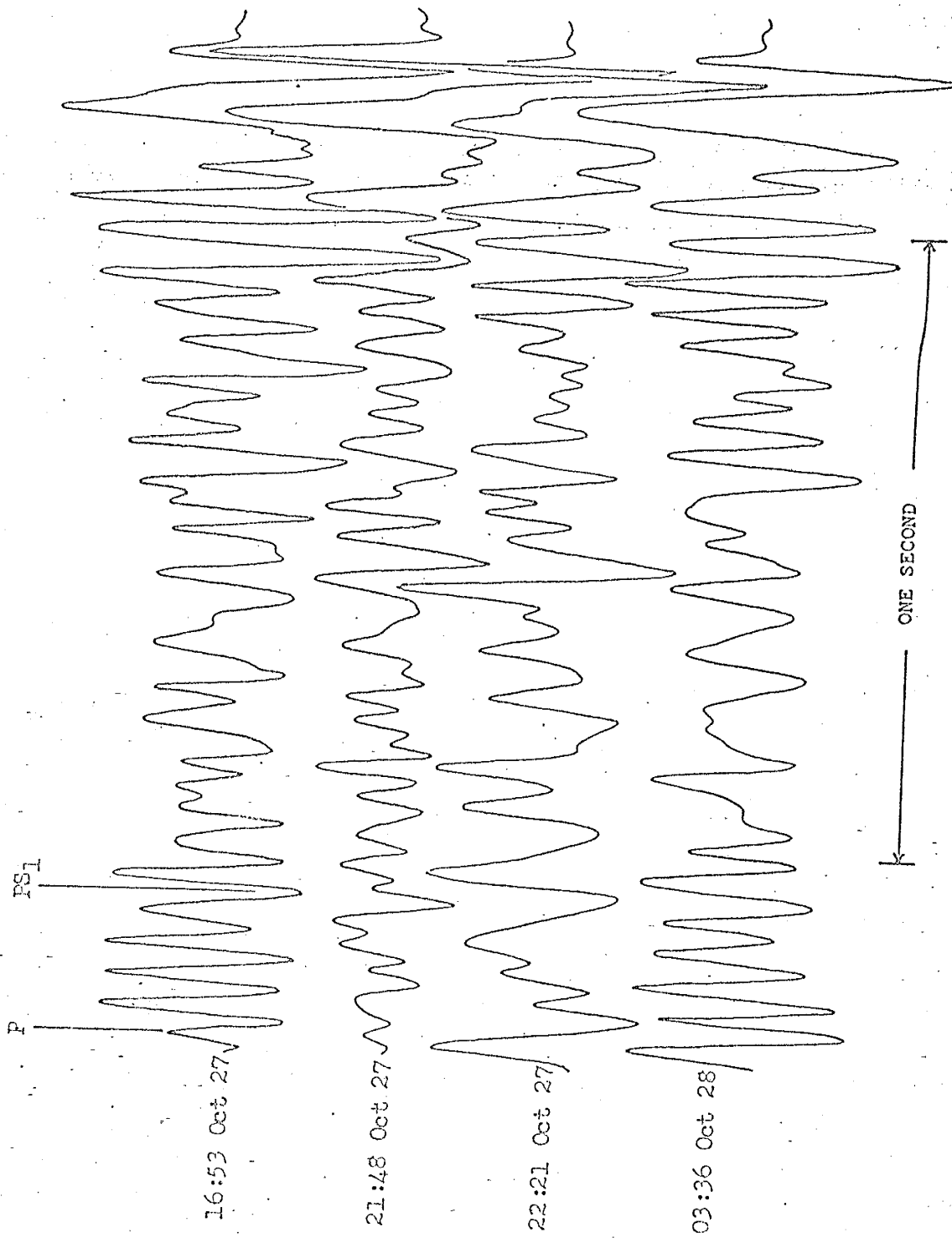Figure 22. Microearthquake traces recorded at NCTH filtered with 0-10 Hz. digital low pass filter.

Figure 33. Microearthquake traces recorded at NM#1 filtered with 10-20 Hz. digital bandpass filter.

77

average calculated depth of the top of the Datil formation (13,000 ft./sec. layer) is 2,100 ft. This is probably a reasonable figure since the 1958 refraction seismograph survey indicates the thickness of the surface layer (7,000 ft./sec.) must be greater than 1,600 ft.

The depth of the microearthquake source was calculated to be 21,300 ft. The distance of the epicenter of the microearthquakes was calculated to be 23,000 ft. These values are also within the range given for Socorro microearthquakes by Sanford and Long.

The fact that the calculated values of the depth of the discontinuity depth of focus, and radius of epicenter based on the PS_1 and SP_1 picks are reasonable lends support to the questionable identification of the PS_1 phase.

EVALUATION OF THE METHOD AS AN EXPLORATION TOOL

LIMITATIONS

The observation and reliable identification of converted energy phases is the most critical aspect of the entire method. In order to be recorded on the seismogram, significant converted wave energy must be generated at the velocity discontinuity in question. This requires that the detector be placed close to the microearthquake source so that the parent waves are fairly strong. The amplitudes of the converted waves are also dependent upon the angle of incidence of the parent wave at the interface. The amplitudes of the horizontal and vertical components of the waves at the surface are dependent upon the angle of incidence of the wave at the surface. These factors serve to geographically restrict the use of the method to those areas for which the position of the detector relative to the source is favorable.

The resolving power of the method is poor when the angles of incidence are high and the velocity contrasts low because of the wide separation along the interface of the points of refraction and conversion. Contrary to other seismic exploration methods, the ability to define small subsurface structures cannot be materially improved by very short station spacing. Therefore the method should not be applied in those areas where the subsurface geology is very complex.

The velocity contrasts required for the generation of usable converted energy phases are higher than the velocity contrasts required for either reflection or refraction seismograph surveys. If the velocity contrast is of the reversed type, interpretation is difficult because the amplitude of converted phases is small.

The accuracy with which seismic phases can be timed is dependent in part on the signal-to-noise ratio, and also upon the frequency of waves.

Recommendations

Two of the most critical requisites of the method are the identification of converted energy arrivals on the seismogram and some knowledge of the velocities. In most instances, the velocity information will be uncertain. However the following recommendations are advanced as a means of increasing the reliability of phase identifications.

1) The signal to noise ratio on the seismogram could be increased by using a multiple seismometer array at each recording station. As shown in a previous development, the signal to random noise ratio improves as N, where N is the number of seismometers in the array. Surface waves could also be effectively cancelled by optimum spacing of the elements of the array.

2) The simultaneous operation of a series of recording stations would provide a subsurface profile from each microearthquake as an aid to correlation. The observed apparent velocity of each wave across the line of seismometer stations could be a criterion for phase identification.

3) Two additional horizontal seismometers should be employed at each station to detect the East-West and North-South components of the ground motion. Then the entire ground motion of any arrival could be reconstructed and the amplitude ratios determined to give an indication as to the type of incoming wave energy. Measurements of the magnitude of the initial motion of each component of the P wave, as it is recorded by each of the three instruments would give an indication of the angle of incidence and azimuth of direct P wave arrivals at the surface.

REFERENCES

Bandat, J., and A. G. Piersol (1966) Measurement and Analysis of
Random Data, John Wiley and Sons, New York, p. 299.

Biles, N. E. (1967) Vertical Ground Motion Showing the Free Surface
Effect, M. S. Thesis, New Mexico Institute of Mining and
Technology, p. 18.

Blackman, R. B. and J. W. Tukey (1958) The Measurement of Power
Spectra, Dover Publications Inc., New York, pp. 14-15.

Fitzsimmons, J. P. (1959) The Structure and Geomorphology of West-
Central New Mexico, Guidebook, New Mexico Geological Society
Tenth Field Conference, p. 14.

Galperin, E. I., and A. V. Forlova (1966) The Study of Converted
Waves by Vertical Seismic Profiling, Izvestiya, Physics of
the Solid Earth, English Edition published by American
Geophysical Union, September, 1966, pp. 93-104.

Grant, F. S. and G. F. West (1965) Interpretation Theory in Applied
Geophysics, McGraw-Hill Book Co., New York, pp. 59-69.

Gutenberg, B. (1944) Energy Ratio of Reflected and Refracted Seismic
Waves, Bull. Seismol. Soc. Am., v. 34, p. 99.

Koefoed, O. (1962) Reflection and Transmission Coefficients for Plane
Longitudinal Incident Waves, Geophysical Prospecting, v. 10,
pp. 305-351.

Lehner, F. E. and F. Press (1966) A Mobile Seismograph Array,
Bull. Seism. Soc. Am., v. 56, pp. 889-897.

Meissner, R. (1965) Multiple Events in Refraction Shooting, Geophysical
Prospecting, v. 13, pp. 647-651.

Mishin, S. V., and N. M. Dareshkina (1966) Isolation of Converted
Waves on Records of Distant Earthquakes, Izvestiya, Physics
of the Solid Earth, English ed. published by Am. Geophys.
Union, pp. 87-92.

Olhovich, V. A. (1964) The Causes of Noise In Seismic Reflection And Refraction Work, Geophysics, v. 29, pp. 395-404.

Robinson, E. A., and S. Treitel (1964) Principles of Digital Filtering Geophysics, v. 29, pp. 395-404.

Sanford, A. R., and C. R. Holmes (1962) Microearthquakes Near Socorro, New Mexico, Jour. Geo. Res., v. 67, pp. 4449-4459.

Sanford, A. R., and L. T. Long (1965) Microearthquake Crustal Reflections Near Socorro, New Mexico, Bull. Seism. Soc. Am., v. 55, pp. 579-586.

Sanford, A. R. (1968) A Gravity Survey in Central Socorro County, New Mexico, New Mexico Bureau of Mines Circular #91, p. 10.

Schind, J. J., J. W. Berg, and K. L. Cook (1960) PS Converted Waves From Large Explosions, Jour. Geo. Res., v. 65, pp. 3817-3824.

Southworth, R. W. (1960) Autocorrelation and Spectra Analysis, Mathematical Methods for Digital Computers, ed. Ralston and Wilf, John Wiley and Sons, New York, pp. 213, 220.

Wengerd, S. A. (1959) Regional Geology as Related to the Petroleum Potential of the Lucero Regional, Guidebook, New Mexico Geological Society Tenth Field Conference, pp. 121-134.

This thesis is accepted on behalf of the faculty of the Institute by the following committee:

Charles R Holmes

A. J. Budding

Allan R. Sanford

Date: _31 Jan 1968_